Sustainable polyethylene fabrics with engineered moisture transport for passive cooling

(Article begins on next page)

16 July 2022

nature portfolio

Supplementary information

Sustainable polyethylene fabrics with engineered moisture transport for passive cooling

In the format provided by the
authors and unedited

Sustainable polyethylene fabrics with engineered moisture transport for passive cooling

Matteo Alberghini[1,2,3], Seongdon Hong[1,4,5], L. Marcelo Lozano[1,6], Volodymyr Korolovych[1], Yi Huang[1], Francesco Signorato[1,2], S. Hadi Zandavi[1], Corey Fucetola[1], Ihsan Uluturk[4], Michael Y. Tolstorukov[7], Gang Chen[1], Pietro Asinari[2,8], Richard M. Osgood III[4], Matteo Fasano[2,3], and Svetlana V. Boriskina[1,*]

[1]*Massachusetts Institute of Technology, Department of Mechanical Engineering, Cambridge, MA, 02139, USA*
[2]*Department of Energy, Politecnico di Torino, Torino, Italy*
[3]*Clean Water Center, Politecnico di Torino, Torino, Italy*
[4]*U.S. Army Combat Capabilities Development Command Soldier Center, Natick, MA, USA*
[5]*Defense Agency for Technology and Quality, Seoul, Korea*
[6]*Tecnologico de Monterrey, Escuela de Ingeniería y Ciencias, Monterrey, Mexico*
[7]*Dana Farber Cancer Institute, Boston, MA, USA*
[8]*INRIM Istituto Nazionale di Ricerca Metrologica, Torino 10135, Italy*

*Corresponding author: sborisk@mit.edu

Table of contents:

1. The Cost and Lifecycle Analysis (LCA) of the polyethylene fibers and fabrics

Polyethylene is one of the most produced materials in the world. Current applications of PE are outside of the textile industry, but the wide availability and low cost of polyethylene make it very competitive with the conventional fiber and textile materials (see Supplementary Table 1).

Supplementary Table 1. Annual production volumes and raw material costs of common textiles.

Material	Silk[1]	Cotton[2,3]	Linen[2,3]	Wool[2,3]	Nylon[2,4]	Polyester[3,4]	Polyethylene[4,5]
Annual production volume (million ton)	0.16	21	0.7	2	59	42	149
Cost (USD per metric ton)	15,000	1540	600-800	20,000 -80,000	2400	1500	<1000

To evaluate the environmental footprint of the polyethylene fabrics and to compare them with the corresponding footprints of other textiles, we calculated the Higg Materials Sustainability Index (MSI) for several common natural and synthetic woven textiles as well as the polyethylene textile[6]. The MSI indices are plotted in Fig. 1a and in Supplementary Fig. 1. In turn, Supplementary Table 2 summarizes the fabrication processes assumed to calculate the MSI index value for each textile type, depending on the material choice.

The Higg MSI is a cradle-to-gate material scoring tool, which addresses impacts that range from the extraction or production of raw materials, through manufacture and finishing, to when the material is ready to be assembled into a final product. The declared unit of the Higg MSI is one kilogram of material. Therefore, the Higg MSI allows the comparison of one kilogram of a specific material to one kilogram of another material. Note that because PE is lighter than other materials, the environmental footprint reduction per equal length of the yarn will be even more pronounced.

Raw Material indices for the fossil fuel-based and recycled polyethylene were taken from the Higg Index plastic database[6]. However, polyethylene is not included in the Higg Index database for the textiles, because it is not currently used as a textile material. However, another olefin polymer – polypropylene – has very similar properties to those of polyethylene and is included in both the plastic and the textile databases. Accordingly, we report the data for the polypropylene Yarn Formation, Textile Formation, and Coloration indices from the Higg textile database in Supplementary Table 2, Supplementary Fig. 1, and Fig. 1a as the estimates for the corresponding

indices for polyethylene. Note that the Raw Material MSI indices for the polyethylene and polypropylene in the plastic database are identical, supporting the validity of the approximation.

According to the measurement conducted by Carbon Trust and the Brazilian Technical Standards Association, polyethylene bio-derived from renewable sources (e.g., sugar cane) has a negative emission footprint (-2.11 kg of CO_2 equivalent per kilogram of product), which was included in the environmental footprint of the Green PE raw material.

Supplementary Table 2. Parameters used to calculate the Higg index of woven textiles.

Material	Silk	Cotton	Linen	Wool	Nylon	Polyester	Polyethylene
Raw material source	Silk, raw, from silkworm	Cotton fiber, conventional production	Flax fiber	Wool, from sheep, fine-medium & superfine, Australia	fossil fuel based		fossil fuel based/recycled /bioderived
Yarn formation	Spinning, for silk	Spinning, cotton, for woven, open end (rotor) (370 DTEX-333 denier-16/1 Ne-27 Nm)	Spinning, bast fiber	Spinning, wool, for woven (370 DTEX-27 Nm)	Extrusion and melt-spinning, continuous filament, no texturing (80 to 500 DTEX-72 to 450 den- 125 to 20 Nm)		
Textile formation	Weaving, 370 DTEX-333 denier-16/1 Ne-27 Nm						
Coloration	Batch dyeing (incl. piece, jet, jig, kier, yarn) - Disperse or cationic dyes						Solution dyeing
Finishing	None						
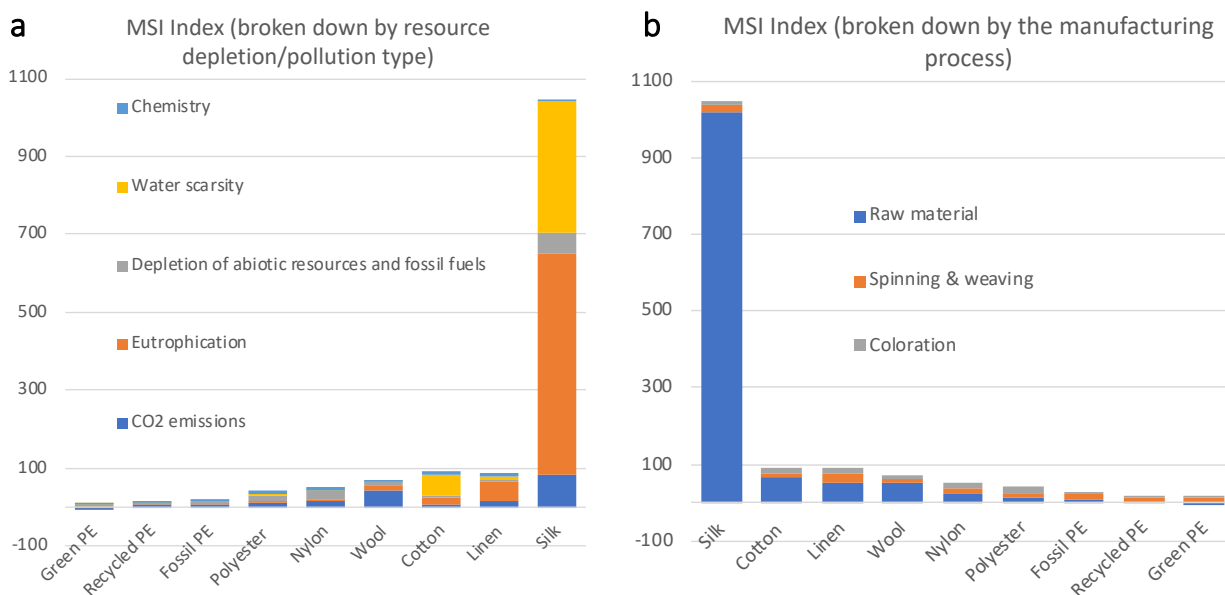
Supplementary Figure 1. Environmental footprint of the textiles during the production (cradle-to-gate) phase. Higg Materials Sustainability Indices (MSI) calculated for 1 kg of woven textiles made from conventional natural and synthetic fibers (see https://msi.higg.org/).

2. Fabrication of the PE fibers, yarns and woven PE textiles

The low linear density polyethylene (LLDPE) multi-filament yarns used in this study have been fabricated on an industrial-scale melt-spin extruder at MiniFibers Inc. (Johnson City, TN). The colored and uncolored polyethylene monofilament fibers composed of either LLDPE or a blend of high-density (HDPE) and ultra-high molecular weight polyethylene (UHMWPE) with mass ratio of 10:90 have been produced by a melt spinning process using a conical miniature twin-screw extruder (MicroCompounder, DACA Instruments) at the U.S. Army Combat Capabilities Development Command Soldier Center (CCDC Soldier Center, Natick, MA). The multi-filament yarns have been woven into a plain-weave textile on an industrial-scale loom at the Shingora Textile Ltd. (Ludhiana, Punjab, India).
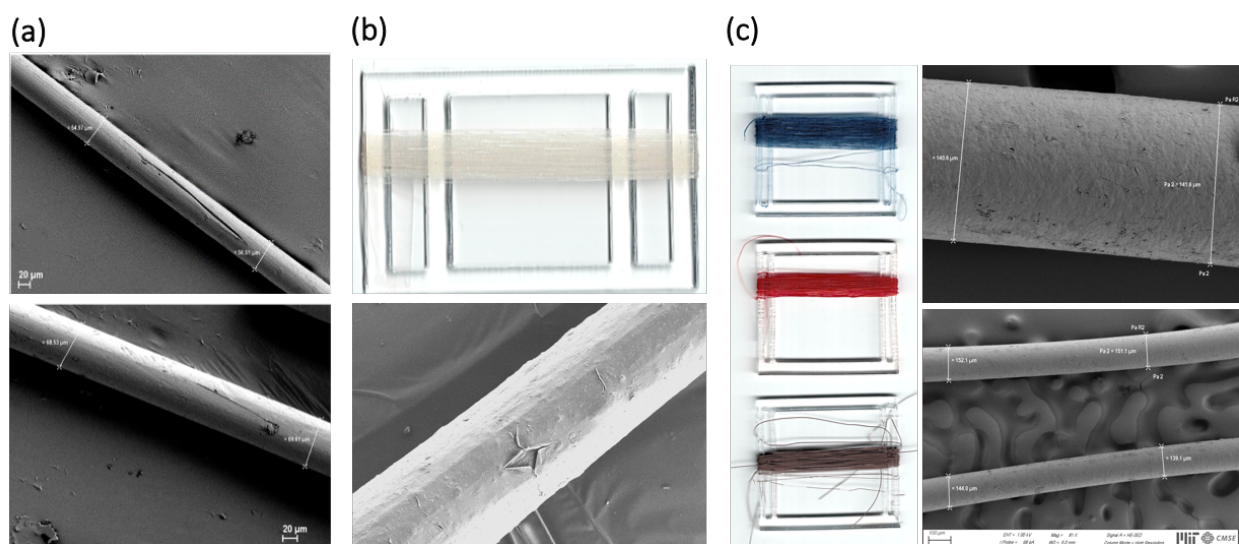
Supplementary Figure 2. Monofilament polyethylene fibers. (a) Scanning electron microscopy (SEM) images of the HDPE monofilament fibers with different diameters produced by varying the melt-spin drawing process parameters. (b) Optical (top) and SEM (bottom) images of the monofilament fiber made of a HDPE-UHMWPE polymer blend. (c) Optical (left) and SEM (right) images of the monofilament fibers with embedded organic dyes (red and blue) and inorganic silicon (Si) nanoparticles of 100 nm in diameter.

3. Structural characterization of polyethylene fabrics

The morphology and structural characterization of the tested fabrics was performed by a high-resolution scanning electron microscope (HR-SEM, Zeiss, model Merlin) operated at 1 kV with a secondary electron detector. For SEM imaging, the samples were coated with a 50 nm-thick layer of carbon. The average fiber diameter was obtained from over 100 measurements performed on the SEM images with the help of the ImageJ software[7].

The SEM images of individual PE fibers, yarns, and the woven PE fabric are shown in Supplementary Figs. 2 and 3a-c. The fine morphology of the PE fiber surface was characterized via

atomic force microscopy (Asylum MFP-3D-BIO) at ambient conditions, using a scan rate of 0.5 - 1.0 Hz (see Supplementary Fig. 3d). The AFM data was analyzed by using the Gwyddion software[8].

The cross-sectional view of the woven PE fabric was obtained with a high-resolution micro-CT scanner (Zeiss Xradia 620 Versa, 0.4x objective), with a resolution of 2 µm/px over 360° rotation and a total scan time of 5 hours. The top-view (a) and the cross-sectional images (b-d) were reconstructed by using the Dragonfly software and are shown in Supplementary Figure 4 and Supplementary Video 1.
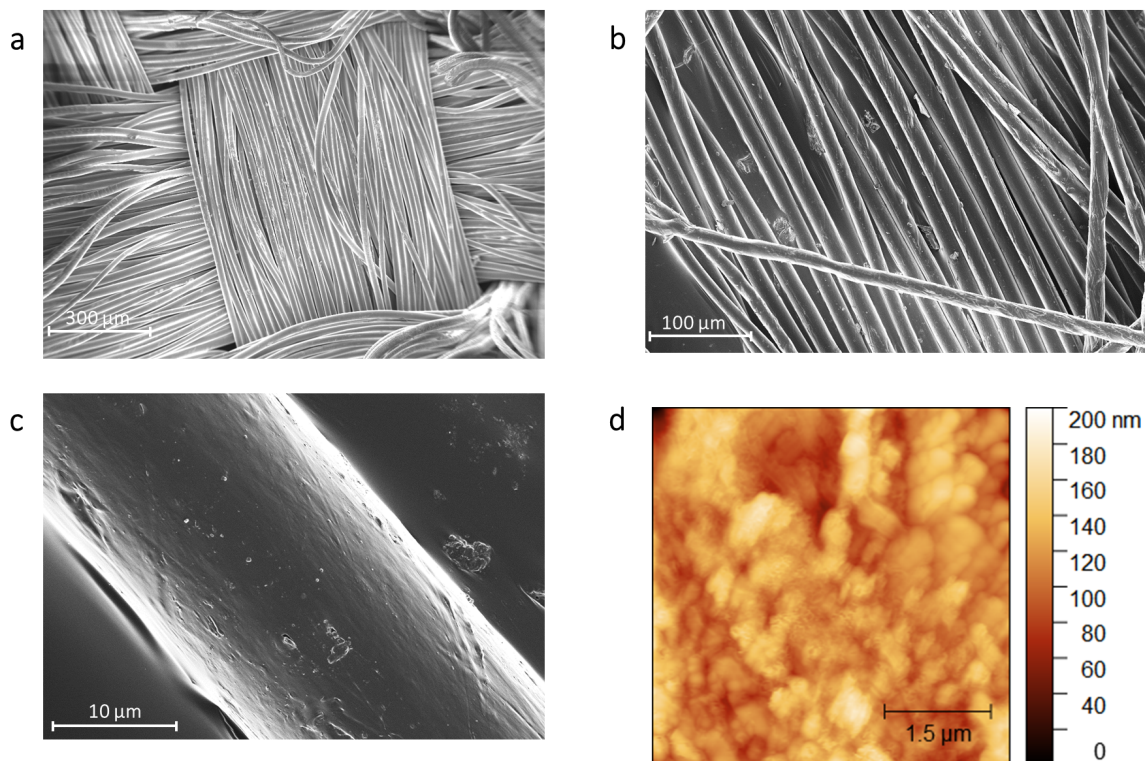
Supplementary Figure 3. Characterization of the multi-filament yarn PE textile and individual fibers. (a-c) SEM images of a woven PE fabric (a), a multi-filament PE yarn (b), and an individual PE fiber filament (c). SEM images have been used to evaluate an average fiber diameter through a probability distribution histogram composed from over 100 observations. (d) The AFM image of the fiber have been used to measure the average roughness of the fibers surface.

4. Evaluation of the average yarn porosity

The average yarn porosity was measured from multiple cross-sectional images obtained via micro-CT measurements. Each slice contains the cross section of four full yarns (see Supplementary Fig. 4b-d). The central parts of each of the four yarns were extracted from the images, paying attention to exclude the fibers on the border of the yarn (see the left cross-section of the Supplementary Fig. 4e). The procedure was repeated for 12 slices, with a pace of 100 µm/slice, for a total of 48 different cross sections. The images were processed with the MATLAB Image Processing Toolbox to obtain binary images as the one reported on the right-hand-side of the Supplementary Fig. 4e. In particular, the function "imbinarize" has been used, which processes the grey-scale input

assigning to each pixel a black-and-white value given an imposed sensitivity level S_0, included in the range from 0 to 1, with higher values of S_0 allowing darker pixels to be recognized as white. Then, the yarn porosity ϕ was computed as the ratio between the number of the white pixels and the total number of the pixels in the image. Consequently, ϕ depends on the set sensitivity level S_0. In the present work, the yarn porosity was computed for each image with a sensitivity level varying in the range from 0.4 to 0.6, with a pace of 10^{-3}. For each value of sensitivity in that range, the yarn porosity was computed and averaged over the results obtained for 48 different images, and the uncertainty of the result was evaluated as the standard deviation of the sample. The results were fitted via the least square method with a first order polynomial in the form: $\phi = a_1 S_0 + a_0$. The reported yarn porosity is evaluated from the fitted curve for $S_0 = 0.5$.
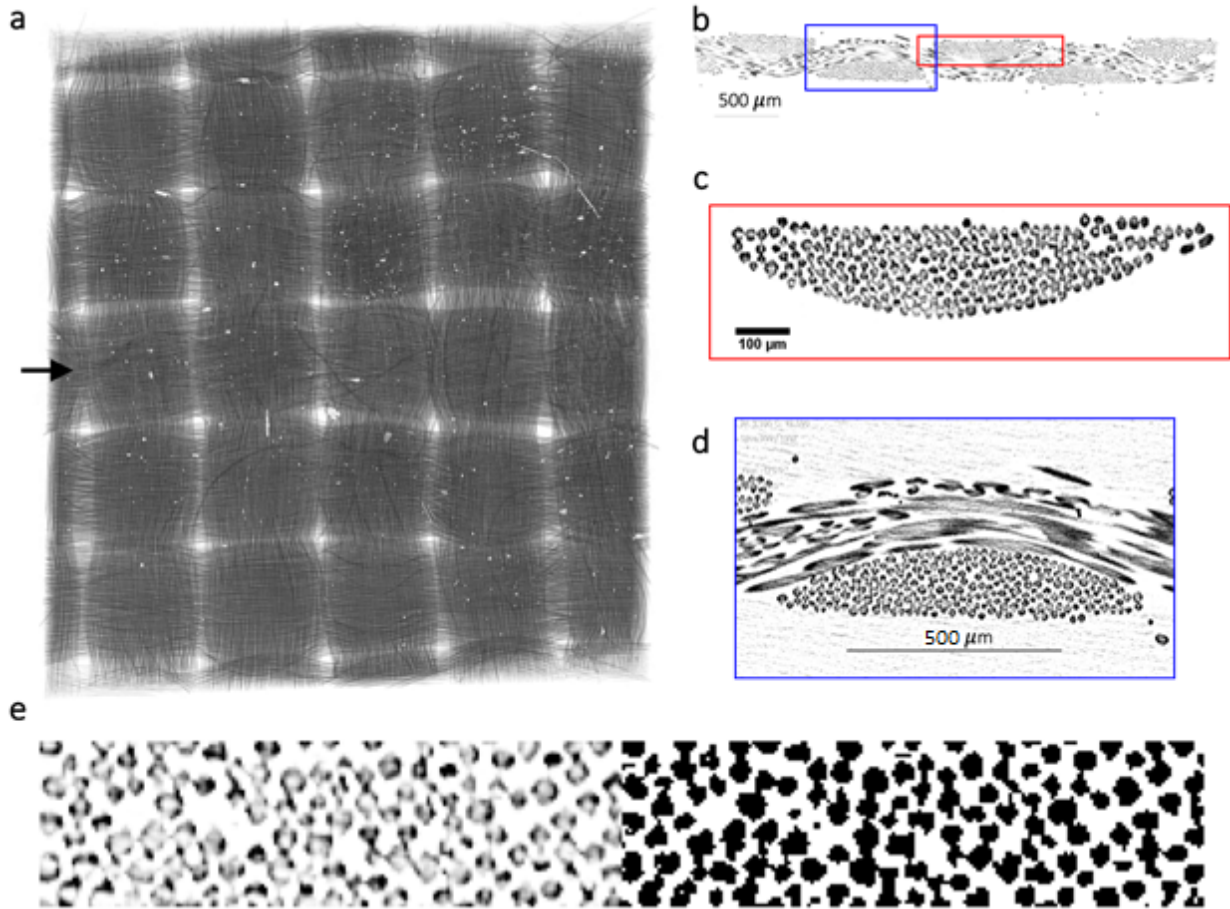
Supplementary Figure 4: Hierarchical structure of the woven polyethylene fabric. (a-d) Micro-CT volume rendering is used to reconstruct the structure of the woven PE (a) by assembling several sections acquired during a 5-hours test. The arrow in panel a highlights one of the cross-sections, which is shown in greater detail in panels c,d, and e to reveal the local structure of the woven fabric. Several images of the yarn cross-section similar to those shown in (c-d) have been analyzed to evaluate the average fiber diameter and yarn twisting. (e) Enlargement of the central part of a yarn section (left) and a high-contrast image processed by the MATLAB code (right), used to compute the average yarn porosity.

5. Measurement of the vertical wicking performance of woven fabrics

The experimental setup (see Supplementary Fig. 5a) for the vertical wicking performance measurement reported in Fig. 2b included two 2.5 cm x 20 cm samples of each material under

investigation (i.e. woven PE, non-woven Tyvek, woven cotton, woven linen, woven polyester), two mechanical vertical stages, a metal bar, a stopwatch, an infrared camera (FLIR ETS320), a caliper (Anytime Tools dial caliper 6"), and a basin filled with distilled water. One end of the metal bar and the water basin were fixed to the stages to tune their relative height. The samples were suspended from the other end of the metal bar by two clips, while the water basin was placed underneath the sample.
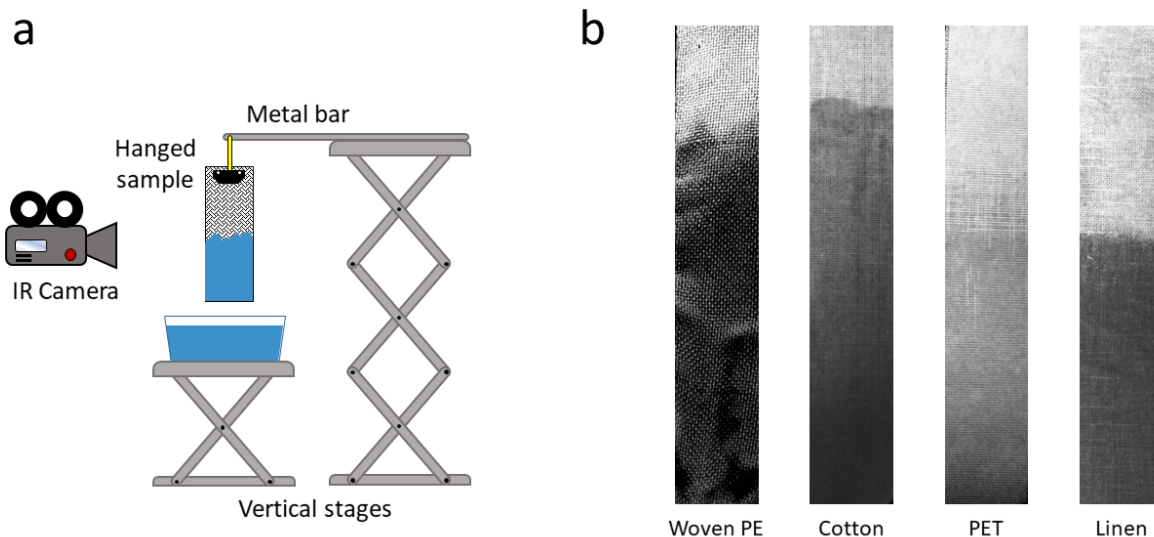
Supplementary Figure 5: Experimental setup to measure the vertical wicking distance according to the AATCC 1977 standard. (a) Schematic of the experimental setup used to evaluate the wicking properties of the fabrics. The fabric samples were attached to a metal bar and partially dipped (approximately 2 mm) in a water basin. The advancing water front could not be seen clearly with the naked eye, and an infrared (IR) camera was used instead to measure its time dependent position. (b) Infrared camera images of the samples of different textiles after a 10-minutes wicking test. The brightness and contrast of the pictures are strongly adjusted to appreciate the exact position of the water front.

The vertical stage underneath the water basin was used to dip approximately 2 mm of the textile sample, and the stopwatch was started. The advancing water front could not be easily observed by a naked eye. Accordingly, the infrared camera was used to locate the position of the water front at the end of the test thanks to the large difference in the infrared emissivity between the wet and the dry textile (see Supplementary Fig. 5b). The height reached by the water front was measured with the caliper. The tests were repeated 3 times for each sample and the results averaged.

Four commercial fabric samples were chosen as references in the wicking test: woven cotton, woven linen, woven polyester, and a non-woven polyethylene material Tyvek (see Supplementary Fig. 6). Woven textiles came in the form of commercial dinner napkins and had comparable thicknesses and the same plane (tabby) weave pattern. The thickness of the woven PE textile was approximately 350 μm, as evaluated from the micro-CT images. The thicknesses of all the studied textiles were also measured by the micrometer (Anytime Tools, Outside Precision), and the data were as follows: woven PE - 310 μm; polyester - 330 μm; cotton - 282 μm; linen - 340 μm; Tyvek - 142 μm (the micrometer thickness measurement returned smaller thickness values than the more accurate micro-CT image measurement because woven fabrics easily deform under pressure). While the reference materials were not exactly identical in composition to the woven

PE textile, they provided reference data for typical wicking properties observed in similar woven textiles without any special surface treatment or added chemistry.

To measure the maximum height reached by the water front, the experimental setup was modified fixing the metal bar on a precision balance (Mettler Toledo, NewClassic MF) placed on the right-hand side vertical stage. The water front was allowed to advance until the effects of viscous friction and gravity balanced the capillary pressure. The weight of the sample during the wicking process was measured by the high-precision balance and the test was considered to have reached a steady state when the standard deviation of 1000 samples was lower than 10^{-3} g, considering a sampling frequency of 3 samples/s. The measurement was repeated on three different samples, and the results were averaged.
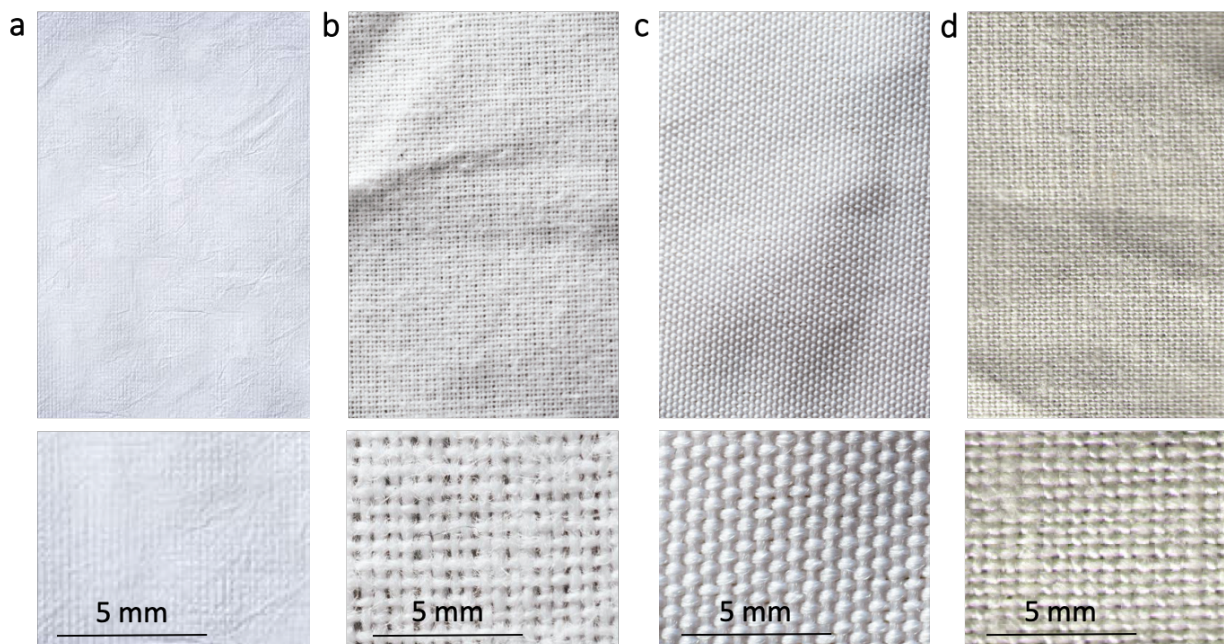
Supplementary Figure 6: Reference conventional fabric samples. Lower- (top) and higher- (bottom) resolution photographs of the commercial textiles chosen as references in the vertical wicking test: (a) non-woven Tyvek PE, (b) woven cotton, (c) woven polyester, and (d) woven linen textiles.
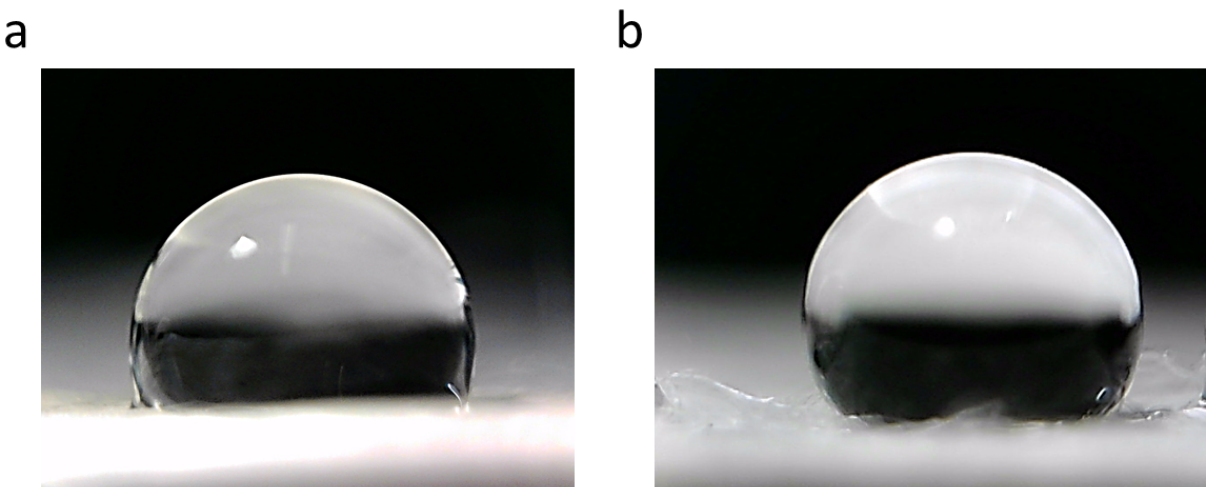
Images of water droplets on the two opposite sides of Tyvek film. The contact angle between water and either of the two surfaces is larger than 90°, confirming the overall hydrophobicity of the material.

6. Surface free energy and contact angle

6.1. Shape parameters of a droplet on a cylindrical fiber

Neglecting the effect of gravity, the equilibrium condition of a droplet on the surface of a fiber requires a constant Laplace's overpressure ΔP over its entire extension[9,10]:

$$\frac{\Delta P}{\gamma_{lv}} = c_1 = \left(\frac{1}{R_1} + \frac{1}{R_2}\right), \tag{1}$$

where γ_{lv} is the water-air surface tension, and R_1 and R_2 are the principal radii of curvature of the droplet surface at a given position. We assume the droplet to be symmetric with respect to the fiber, as the one displayed in Fig. 2c, thus allowing to use this symmetry to simplify the mathematical formulation. According to this simplification, only images of symmetrical droplets were used to evaluate the average water-fiber contact angle from experimental measurements.

Referring to Supplementary Fig. 8a, the two principal radii of curvature are identified by the segments AN, in the plane of the figure, and AM, in the plane containing the segment and perpendicular to the figure. Thus:

$$AN = R_1 = \frac{x}{\sin\phi}, \qquad AM = R_2 = \frac{ds}{d\phi}. \tag{2}$$

See Supplementary Fig. 8a for definitions of parameters $x, \phi,$ and s. Substituting Supplementary Eq. 2 in 1, it can be rewritten as:

$$c_1 = \frac{\sin\phi}{x} + \cos\phi \frac{d\phi}{dx} = \frac{1}{x}\frac{d}{dx}(x\sin\phi), \tag{3}$$

Supplementary Eq. 3 can be integrated as:

$$\frac{c_1 x^2}{2} + c_2 = x\sin\phi, \tag{4}$$

where the constants c_1 and c_2 can be computed considering the boundary conditions:

$$x|_{z=0} = T/2, \qquad \phi|_{z=0} = \pi/2 \tag{5}$$

$$x|_{z=L/2} = r, \qquad \phi|_{z=L/2} = \pi/2 - \theta$$

obtaining the final form:

$$\sin\phi = \left(\frac{r\cos\theta - T_1}{r^2 - T_1^2}\right)x + \frac{1}{x}T_1 r\left(\frac{r - T_1\cos\theta}{r^2 - T_1^2}\right), \tag{6}$$

where $T_1 = T/2$. See Supplementary Fig. 8b for definitions of parameters $T, L,$ and r. Referring to Supplementary Fig. 8a, the derivative of the droplet profile can be expressed as:

$$\frac{dx}{dz} = -\frac{1}{\tan\phi} = -\frac{\sqrt{1 - \sin^2\phi}}{\sin\phi}. \tag{7}$$

Supplementary Eq. 6 is used to express $\sin\phi$; Supplementary Eq. 7 is the differential equation describing the droplet profile. Thus, the length of the droplet can be computed as:

$$L = 2 \int_0^{L/2} \mathrm{d}z = 2 \int_r^{T/2} \frac{\sin\phi}{\sqrt{1 - \sin^2\phi}} \, \mathrm{d}x. \tag{8}$$

Supplementary Eqs. 6-8 can be used in an iterative procedure to compute the contact angle of a symmetric water drop on a fiber given its shape parameters, namely the fiber radius r, the droplet thickness T and length L (see Supplementary Note 7).
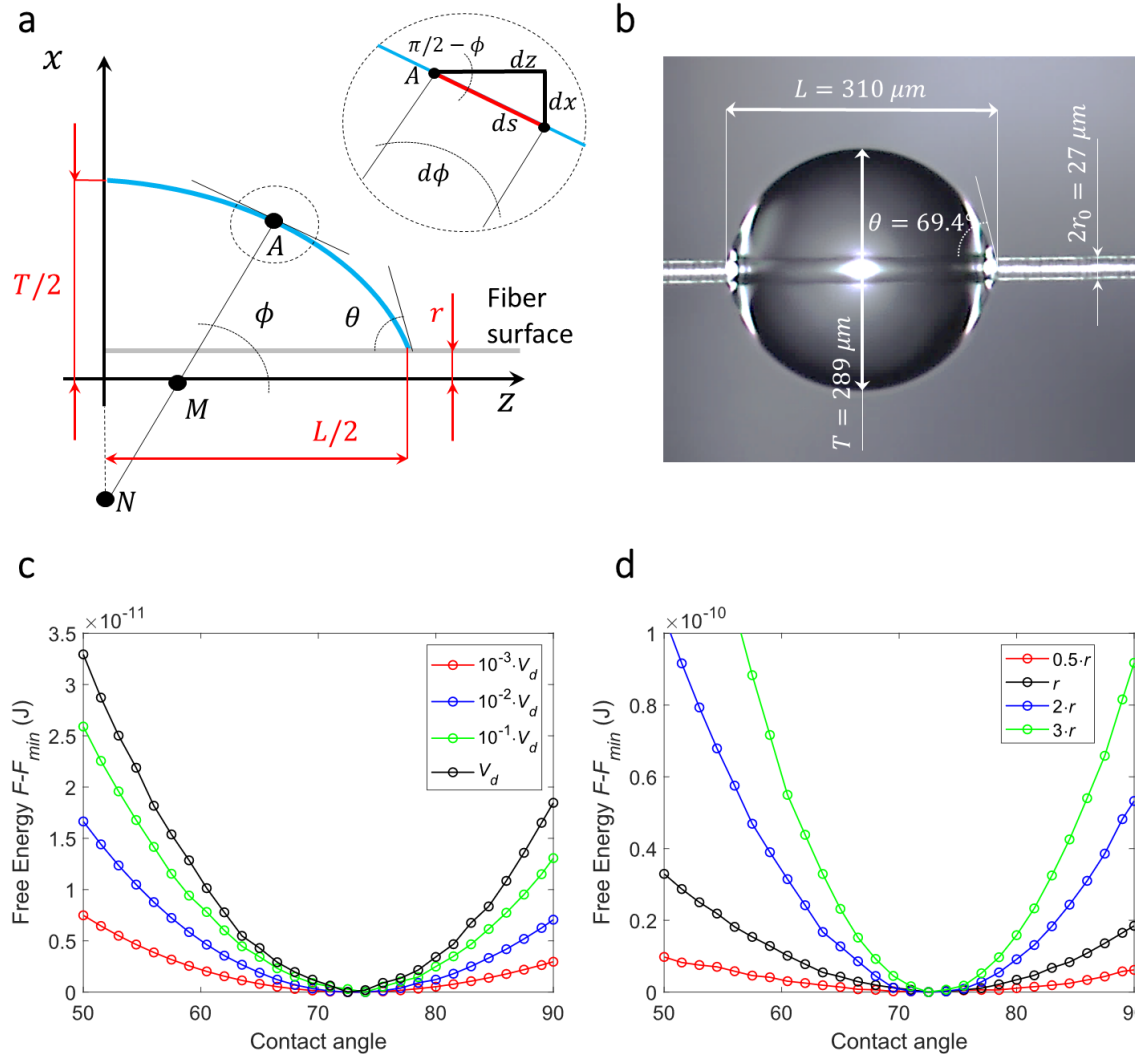
Supplementary Figure 8: Equilibrium contact angle and free energy of a drop on a fiber. (a) Schematics of a droplet on a fiber. If the droplet is sufficiently small to neglect the effect of gravity, its two planes of symmetry can be used to simplify the derivation of the differential equation describing its profile. (b) The fiber radius, the droplet thickness and length can be evaluated from microscope images to compute the water-fiber contact angle from Supplementary Eqs. 6-8 through the procedure described in Supplementary Note 7. To maintain pertinence with the case of study, the fiber radius r and the droplet volume V_d used to compute the theoretical equilibrium contact angle between a water droplet and a nylon fiber in Supplementary Note 6.2, were evaluated from the shape parameters shown in this picture. (c-d) Free energy of a water droplet on a nylon fiber. The black dashed curves are obtained for $\gamma_{lv} = 72.8 \, mN/m$, $\gamma_{sv} = 41.4 \, mN/m$, $r = 13.5 \, \mu m$ and $V_d = 1.29 \cdot 10^{-11} \, m^3$. The droplet volume (c) and fiber radius (d)

on the surface do not affect the value of the equilibrium contact angle, which is only determined by the surface tensions at the contact line, but change the free energy landscape, making it steeper for larger droplets on larger fibers.

The external surface of the water droplet can be computed as:

$$A_d = 2\pi \int_{-\frac{L}{2}}^{\frac{L}{2}} \frac{x}{\sin \phi} \, dz = 4\pi \int_{\frac{T}{2}}^{r} -\frac{x}{\cos \phi} \, dx \, , \tag{9}$$

which can be numerically integrated recalling that $\cos \phi = (1 + \tan^2 \phi)^{-0.5}$ and considering Supplementary Eqs. 6 and 7 to express $\tan \phi$ as a function of the droplet profile x. Similarly, the volume of the droplet can be computed as:

$$V_d = \pi \int_{-L/2}^{L/2} x^2 dz - V_{df} = 2\pi \int_{\frac{T}{2}}^{r} -x^2 \tan^2 \phi \, dx - V_{df} \, , \tag{10}$$

where $V_{df} = \pi r^2 L$ is the volume of the fiber surrounded by the droplet.

6.2.   Numerical evaluation of the surface free energy

In the present paragraph, the subscripts l, v and s refer to the three-phases composing the system: the liquid drop, the vapor-gas mixture surrounding the others, namely air, and the solid fiber, respectively. On ideal, planar surfaces, the equilibrium condition at the three-phases contact line can be described by the Young's equation[11,12]:

$$\gamma_{sv} - \pi_e = \gamma_{sl} + \gamma_{lv} \cos \theta_e \, , \tag{11}$$

where γ_{lv} is the surface tension of the liquid drop immersed in air, γ_{sv} is the surface tension of the fiber immersed in air, γ_{sl} is the fiber-liquid surface tension and π_e is the equilibrium pressure of adsorbed vapor of the liquid on the surface, which can usually be neglected for polymers with low surface free energy[11]. The surface tension is composed by two components: $\gamma = \gamma^d + \gamma^p$, where γ^d is the dispersive component (due to the London forces) and γ^p the polar component (due to the hydrogen bonding and dipole-dipole interaction). According to the method proposed by Owens, the surface tension of the solid substrate can be computed from the adhesion energy as[11,13]:

$$\gamma_{sl} = \gamma_{lv} + \gamma_{sv} - 2 \left(\sqrt{\gamma_{sv}^d \gamma_{lv}^d} + \sqrt{\gamma_{sv}^p \gamma_{lv}^p} \right) , \tag{12}$$

which, combined with Supplementary Eq. 11, allows to compute the equilibrium contact angle on a planar surface as a function of their surface tensions:

$$\theta_e = \text{acos} \left(2 \frac{\sqrt{\gamma_{sv}^d \gamma_{lv}^d} + \sqrt{\gamma_{sv}^p \gamma_{lv}^p}}{\gamma_{lv}} - 1 \right). \tag{13}$$

Considering pure water in air, with $\gamma_{lv} = 72.8 \, mN/m$ and $\gamma_{lv}^p = 51.0 \, mN/m$,[14] only surfaces with predominantly polar surface tension are strongly hydrophilic. Supplementary Eq. 13 can be used to compute θ_e of a water droplet on an ideal, planar surface. As an example, nylon 6.6, a common material in textile industry, presents[14] $\gamma_{sl}^d = 33.7 \, mN/m$ and $\gamma_{sl}^p = 7.8 \, mN/m$, which results in a weak hydrophilicity with $\theta_e = 73.1°$. On the other hand, PE has a similar dispersive component, while lower polar surface tension[14] $\gamma_{sl}^p = 1.1 \, mN/m$, resulting in a weak hydrophobicity with $\theta_e = 94.4°$.

To evaluate the effect of the fiber shape on its surface energy and the resulting contact angle, we consider a nylon fiber in the following discussion. Since the flat surface of nylon is already hydrophilic, we calculate the expected change in the contact angle caused by the fiber surface deviation from the planar surface. We consider a liquid drop on a cylindrical fiber, whose free energy F can be evaluated as:

$$F = 2\pi r(L' - L)\gamma_{sv} + A_d\gamma_{lv} + 2\pi rL\gamma_{sl} \,, \tag{14}$$

where r and L' are the radius and total length of the fiber, A_d and L are the surface area and length of the liquid droplet. The three terms in the right-hand side of Supplementary Eq. 14 account for the contributions of the dry fiber, the shape of the drop and the solid-liquid interface to the total F of the dry fiber, respectively. Supplementary Eq. 14 can be re-arranged to neglect the initial F of the dry fiber, constant for any configuration of the drop[15]:

$$F = A_d\gamma_{lv} + A_{df}(\gamma_{sl} - \gamma_{sv}) \,, \tag{15}$$

where $A_{df} = 2\pi rL$ is the cylindric liquid-solid contact surface. Thus, considering a drop with a fixed volume V_d and surface tension γ_{lv}, its equilibrium contact angle θ_e on a fiber with a given γ_{sl} is determined by the minimization of Supplementary Eq. 15, according to the second principle of thermodynamics.

We investigated the influence of the fiber radius r, droplet volume V_d and surface tension on the equilibrium contact angle θ_e. A MATLAB routine has been implemented to compute F_i for each θ_i in the range between 0° and 90°. For each θ_i in that range, the routine computes the shape parameters L_i and T_i from Supplementary Eqs. 6-8, with the constraint of observing the conservation of the droplet volume, namely $V_{d_i} = V_d$, where the droplet volume V_{d_i} can be computed from Supplementary Eq. 10. The volume conservation implies that lower values of θ_i result in flattened drops and higher solid-liquid contact area, while higher values of θ_i lead to sphere-like drops and lower solid-liquid contact area. Once the shape parameters L_i and T_i are determined for a given θ_i, the surface area of the droplet A_{d_i} can be computed from Supplementary Eq. 9 and the solid-liquid contact area as $A_{df_i} = 2\pi rL_i$. These values can be substituted into Supplementary Eq. 15 to compute F_i. As previously described, θ_e is unique and identified as the θ_i minimizing F.

This procedure requires to select a fiber radius r and a droplet volume V_d, besides the surface tensions of the materials involved, to compute θ_e. To be pertinent with the fibers proposed in this work, we evaluated r and V_d from the image of the water drop shown in Supplementary Fig. 8b. Note that any other pair of parameters r and V_d within the validity range of the hypothesis of negligible effect of gravity can be used. Thus, multiples and submultiples of r and V_d were used to evaluate their effect on θ_e. Given the shape parameters $r = 13.5 \, \mu m$, $L = 310 \, \mu m$ and $T = 289 \, \mu m$ measured from the microscope image, its contact angle $\theta_e = 69.4°$ was computed from

Supplementary Eqs. 6-8 through the procedure described in Supplementary Note 7, while its volume $V_d = 1.29 \cdot 10^{-11} \, m^3$ was evaluated from Supplementary Eq. 10. The capillary length for water[9] $\kappa = \sqrt{\gamma_{lv}(\rho g)^{-1}} = 2.7 \, mm$ is larger than L and T, thus the hypothesis of negligible effect of gravity is valid.

Supplementary Figs. 8c,d explore the effect of the droplet volume and fiber radius, respectively, on the FE of a system composed by a water drop with $\gamma_{lv} = 72.8 \, mN/m$ on a nylon 6.6 fiber with $\gamma_{sv} = 41.4 \, mN/m$. To simplify the representation, the curves were shifted downwards by their minimum value. The black lines are obtained for $V_d = 1.29 \cdot 10^{-11} \, m^3$ and $r = 13.5 \, \mu m$. It can be observed that the minimum of the FE is localized at $\theta_e = 73.3°$, approximately the same value obtained from Supplementary Eq. 13 for a water drop on an ideal planar surface of nylon. This result is consistent with the hypothesis of Carrol[10] and the results reported by Extrand *et al*[16]. Furthermore, different values of V_d and r do not modify the equilibrium contact angle θ_e but only affect the free energy landscape, making it steeper for larger droplets and fibers, thus hindering deviations from the equilibrium configuration. On the contrary, on a more hydrophilic fiber, such as glass, characterized by[17] $\gamma_{sv} = 70.5 \, mN/m$, $\gamma_{sv}^p = 47.5 \, mN/m$ and an equilibrium contact angle with water of approximately 15° and under the assumption of $\pi_e = 0$, smaller droplet size results in a steeper free energy landscape, coherently with the results of McHale[18]. Thus, the analysis performed proved that the water-fiber equilibrium contact angle is not influenced by the fiber radius r or drop volume V_d but is uniquely determined by the surface tensions of the materials involved. Furthermore, its value is the same as the one evaluated on an ideal planar surface, calculable via Supplementary Eq. 13.

7. Experimental evaluation of the water-fiber contact angle

The water-fiber contact angle was experimentally evaluated from Supplementary Eqs. 6-8 by measuring the height and length of a droplet deposited on a fiber (see Fig. 2c). Considering as initial guess values $\theta_{g_1} = 1°$ and $\theta_{g_2} = 90°$, we used a MATLAB code to solve iteratively Supplementary Eqs. 6-8 until the predicted drop length is equal to the value of L experimentally evaluated, given a threshold tolerance $\varepsilon = 10^{-4}$. The resulting value of θ was compared with the results obtained through the method proposed by Carrol[10] and Kralchevsky[19], finding a discrepancy within 0.1%.

a

150 µm

b

150 µm
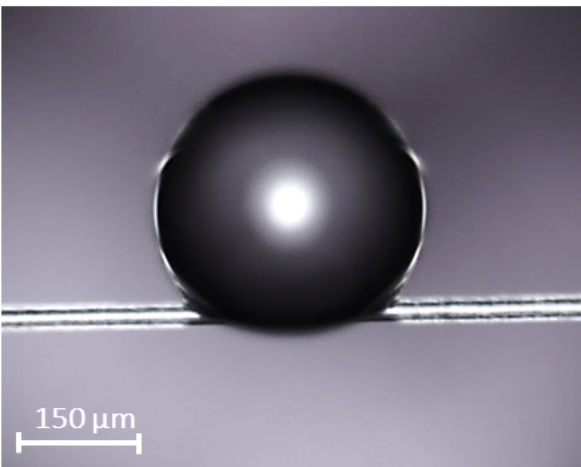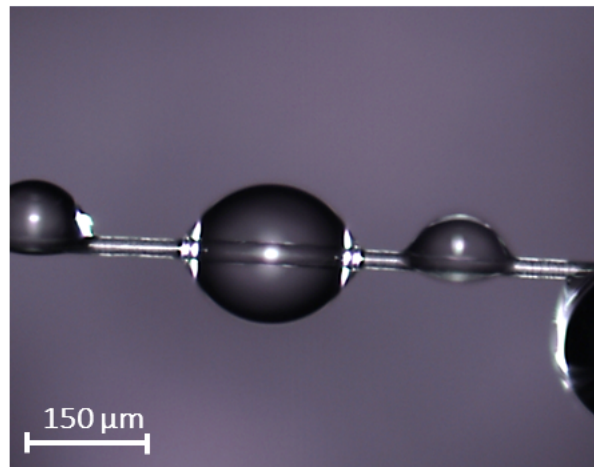
Supplementary Figure 9: Wettability properties of the PE fibers. Despite presenting an overall weak hydrophilicity, the same fiber may present zones of both strong hydrophobicity (a) and good hydrophilicity (b), demonstrating uneven surface properties.

The fibers were extracted from randomly picked yarns in woven PE fabric samples. The extremities of each fiber were fixed with tape on two glass slides. Water was sprayed above the setup to allow the deposition of water droplets on the surface of the fiber. A confocal microscope coupled to a Raman spectrometer (Horiba, LabRAM HR Evolution) was used to observe and photograph the droplets deposited on the fibers. The effect of evaporation was reduced by limiting the air speed in the proximity of the microscope objective. Then, the contact angle of each droplet was measured a second time, by taking the second photograph 20 seconds after the first one. Conservatively, the maximum value between the two measurements was accepted if the variation (due to evaporation) was lower than 5%. A maximum of two droplets per each fiber were photographed before replacing the sample. The contact angle reported was obtained by averaging the measures from more than 16 droplets per each tested material.

8. Surface chemistry of the fibers: plasma treatment, FTIR, and XPS analyses

The homogeneity of the PE fiber surface and its hydrophilicity (see Supplementary Fig. 9) can be improved by plasma treatment. To evaluate the efficiency of such treatment, woven PE fabric samples were treated with a plasma cleaner from Harrick Plasma (model PDC-32G) with a maximum Radio Frequency (RF) power of 18W, in an oxygen environment and three different durations of treatment, namely 1, 3 and 10 minutes. The chamber of the plasma cleaner was initially purged two times with oxygen. After the purge, the woven PE sample was placed inside the reaction chamber under an oxygen flow suitable to set the pressure inside the chamber in the range of $800-1000$ mTorr, which was around 0.85 SCFH. Afterward, the RF radiation was turned on at the maximum power during each treatment time (i.e., 1, 3 or 10 minutes). The 10-minute treatment was done in two steps, 5 minutes each, to avoid the overheating of the instrument. After the time has elapsed, the RF was turned off, the oxygen flow was closed, and the chamber was vented with Nitrogen.

Three woven PE samples were treated with low-power oxygen plasma (16 W), and the modified contact angle was measured on several fibers per sample. The results are plotted in Supplementary Fig. 10a for three different exposure times, 1 minute (P1), 3 minutes (P3) and 10 minutes (P10). The resulting contact angles are $(60.8 \pm 3.8)°$, $(54.6 \pm 2.6)°$ and $(51.9 \pm 4.3)°$, respectively. The corresponding data for the pristine PE films and the untreated as-spun woven PE yarns (P0) are also shown for comparison. The results show that a short treatment with a low-power source allows obtaining homogenous surface hydrophilicity, while longer exposure times do not yield further significantly-significant decrease of the contact angle, in agreement with prior studies[20,21].

The surface chemistry of fibers comprising the woven PE fabrics was probed via the Fourier Transform Infrared (FTIR) spectroscopy, using the Attenuated Total Reflectance (ATR) mode. For this, a Nicolet 6700 spectrometer equipped with a Nicolet Continuμm Microscope with an ATR objective with Germanium crystal was used. After visually selecting the desired area for analysis, the Germanium ATR crystal was moved into place and the sample stage was raised so that the contact was made with the fabric surface. The contact pressure was controlled by a pressure

monitoring device to ensure reproducibility of the results. ATR-FTIR spectra were collected in the range 4000-650 cm^{-1} at resolution of 4 cm^{-1} and were averaged over 32 scans. The FTIR spectra of the plasma treated fibers exhibit a weak spectral feature at the wavelength corresponding to the C-O molecular bond, which indicates a fiber surface modification by the oxygen-containing functional groups (Supplementary Fig. 10b).
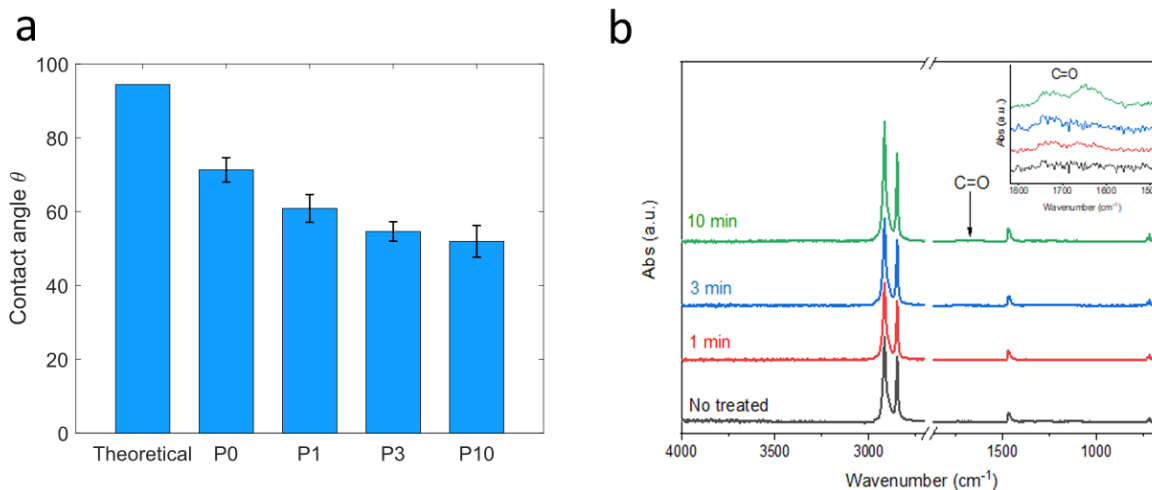

Supplementary Figure 10: Surface properties of the PE fibers. (a) The experimentally measured contact angle between water and plasma-treated PE fibers compared to a reference value for a pristine material, obtained from the theoretical model shown in Supplementary Note 6.2. Gradual increase of the PE fiber hydrophilicity via low-power plasma treatment can be achieved (P0-P10 labels correspond to 0, 1, 3 and 10 minutes of exposure to plasma treatment, respectively). (b) Oxidation of the fiber surface is verified by the attenuated total reflection (ATR) FTIR spectroscopy, showing a minor modification of the functional groups on the surface. The inset highlights the wavelength band between 1500 cm^{-1} and 1800 cm^{-1}, corresponding to the C=O stretching bond, where the treated fibers show an enhanced absorption, proving the effectiveness of the treatment.

We have performed additional analysis of the surface oxidation of the PE fibers by using the X-ray photoelectron spectroscopy (XPS). We have used the Physical Electronics Versaprobe II X-ray Photoelectron Spectrometer to perform elemental and chemical spectroscopic analysis of fiber surfaces. Monochromatic Al Kα radiation (hν = 1486.6 eV) was used as the excitation source to analyze the different binding energy peaks (pass energy 11 eV, analyzer resolution ≤0.5 eV). Low energy Ar+ ion gun and low energy neutralizer electron gun were used to minimize charging on the surface. The samples of woven fabrics and PE yarn were analyzed in an ultra-high vacuum chamber, and the results are summarized in Supplementary Fig. 11.

In addition to characterizing the woven PE fabrics, we also characterized the LLDPE yarn, which has not been subjected to twisting, plying, knitting, weaving or washing. The tested yarn has been fabricated several months later than the yarn used to weave the PE fabrics. The XPS measurements revealed higher atomic concentration and molecular weight % of oxygen extracted from the XPS spectra of the PE yarn than from the spectra of the woven fabric. This observation confirms the hypothesis that the oxidation occurs at the fiber production stage and persists for months and years. As we have demonstrated, PE fiber oxidation may be reduced in the process of wetting and air drying but hydrophilicity can be restored by oxygen plasma treatment and even by a simple

fabric hand-rubbing process.
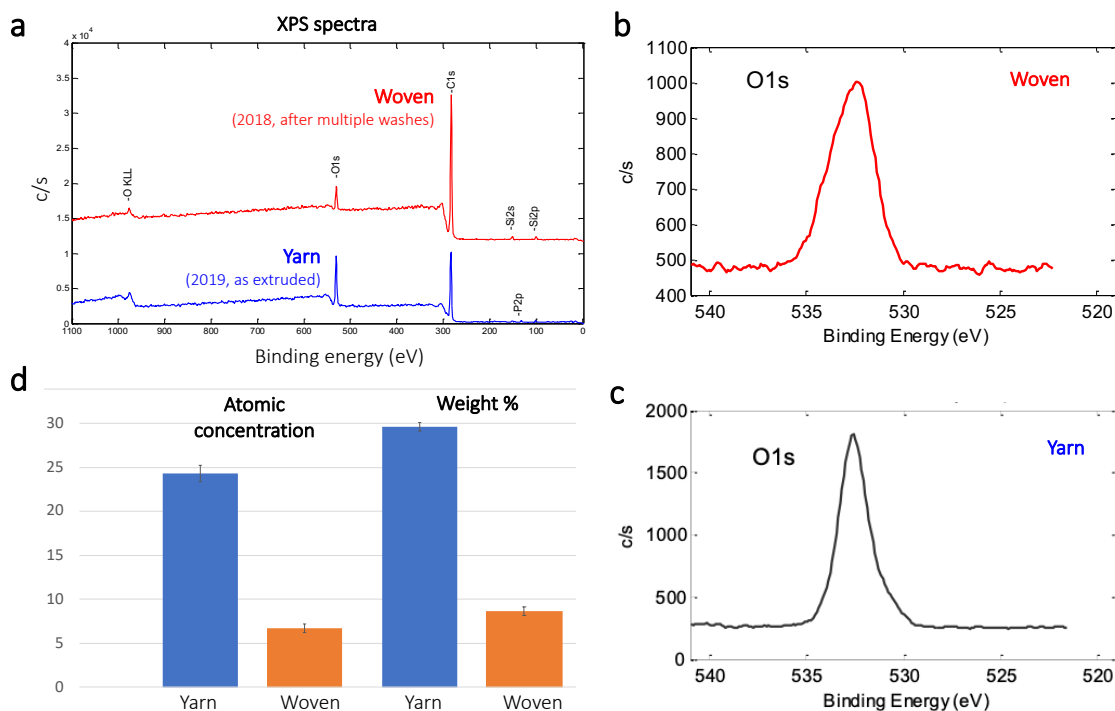
Supplementary Figure 11. The X-ray photoelectron spectroscopy (XPS) reveals fiber oxidation at the extrusion step, which may be reduced by fabric weaving and washing processes. (a) XPS spectra of the PE yarn, which was extruded at the beginning of 2019, kept on the bobbin and never washed/used (blue) and the woven fabric made from the same type of yarn extruded several months earlier in 2018 (red), after multiple fabric washing cycles. (b) An example of the high-resolution XPS oxygen peak in the woven fabric spectrum. (c) An example of high-resolution XPS oxygen peak in the yarn spectrum. (d) The average values of the atomic concentration and molecular weight % of oxygen extracted from the XPS spectra of the PE yarn (blue) and the woven fabric (orange). XPS measurements were conducted in September 2020.

9. Calculation of the average surface tension of the PE fibers. Maintenance and restoration of the fabric hydrophilic properties

According to the results presented in Supplementary Note 6.2, pristine PE is weakly hydrophobic, presenting a theoretical equilibrium contact angle with water of $\theta_e = 94.4°$ when cast as either a planar or a cylindrical surface. However, the experimental evaluation of the water-fiber contact angle was $\theta = (71.3 \pm 3.3)°$, lower than the theoretical value, and inhomogeneous along the same fiber (see Supplementary Fig. 9). Furthermore, the chemical characterization of the fibers surface through FTIR-ATR spectroscopy, presented in Supplementary Note 8, highlighted only the absorption peaks of pure PE, proving the purity of the bulk material used to cast the fibers. Thus, we concluded that the surface of the fibers was weakly functionalized during the fabrication process by a low degree of oxidation and the presence of surface charges[22].

Supplementary Note 6.2 demonstrated that, given the surface free energy of a liquid drop on a solid substrate immersed in air, the equilibrium contact angle for planar or cylindrical surfaces is only determined by the surface tension of the materials. Thus, we can iteratively solve

16

Supplementary Eq. 13 increasing the polar component of the surface tension (γ_{sv}^p), which is responsible for the hydrophilic interactions, until the predicted equilibrium contact angle (94.4°) is equal to the experimental one (71.3°). According to this procedure, γ_{sv}^p increases from $1.1\ mN/m$ to $9.4\ mN/m$, for a total surface tension of $\gamma_{sv} = 40.7\ mN/m$, approximately 25% larger than the theoretical value of pristine PE and similar to the surface tension of nylon.

However, the functionalization of the PE fibers is not permanent, as demonstrated by repeating multiple times the 10-minutes vertical wicking test described in Supplementary Note 5 on the same woven PE sample. As it can be observed in Supplementary Fig. 12, the height reached by the water front h_{10} decreases each repetition, proving progressive decrease of the fibers surface tension, in agreement with other observations of charged insulators exposed to water[23].
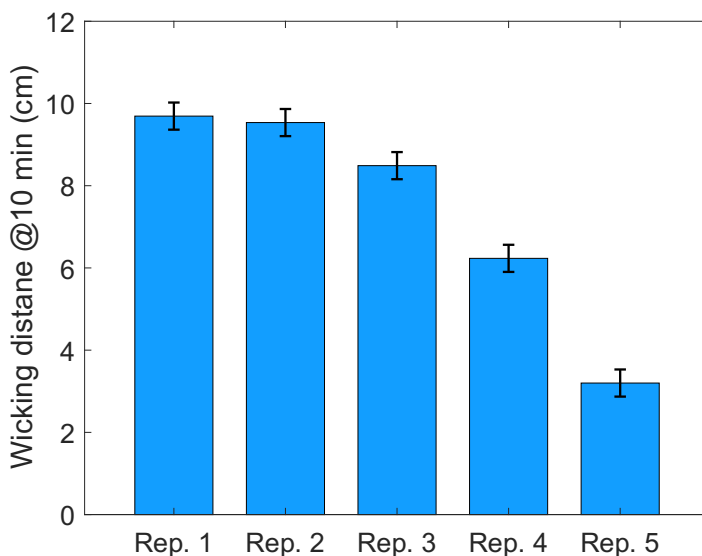
Supplementary Figure 12: Durability of the hydrophilicity of the PE fabric. The vertical wicking tests are repeated five times on the same sample to evaluate the durability of the surface functionalization provided by the fabrication process. The progressive decrease of the height reached by the water front can be ascribed to the progressive reduction of the fibers surface tension when put in contact with water. The performances remain stable for 3-4 cycles before degrading.

However, the hydrophilicity of the woven PE can be restored by repeat oxidation in the presence of oxygen even at ambient temperatures,[19,20] e.g., due to exposure to UV light in the solar spectrum. We tested the durability of the woven PE fabric under exposure to the UV light and the role of the UV exposure in the restoration of the hydrophilicity of the material. Two textile samples subjected to multiple washing and drying cycles and not exhibiting wicking performance have been chosen for this experiment. One sample was placed within a closed polystyrene box and exposed to UV light (Vilber VL-6.C, wavelength: 254nm, total power: 6 W, specific power: 710 μW/cm^2) for approximately 335 hours (two weeks), while the second sample was stored in a Nylon bag in dark conditions, and used as reference. The temperature within the aging box was (28.5 ± 0.5) °C for the entire duration of the test. As expected, the exposure time and the irradiated power was sufficient to cause a visible yellowing of the polystyrene box (see Supplementary Fig. 13a), while it did not affect the colour of the woven PE sample (see Supplementary Fig. 13b). The structures of the fabrics were also inspected with an optical microscope (KERN OBL 155, 10x lens) and no significant differences could be observed (see Supplementary Fig. 13c,d).
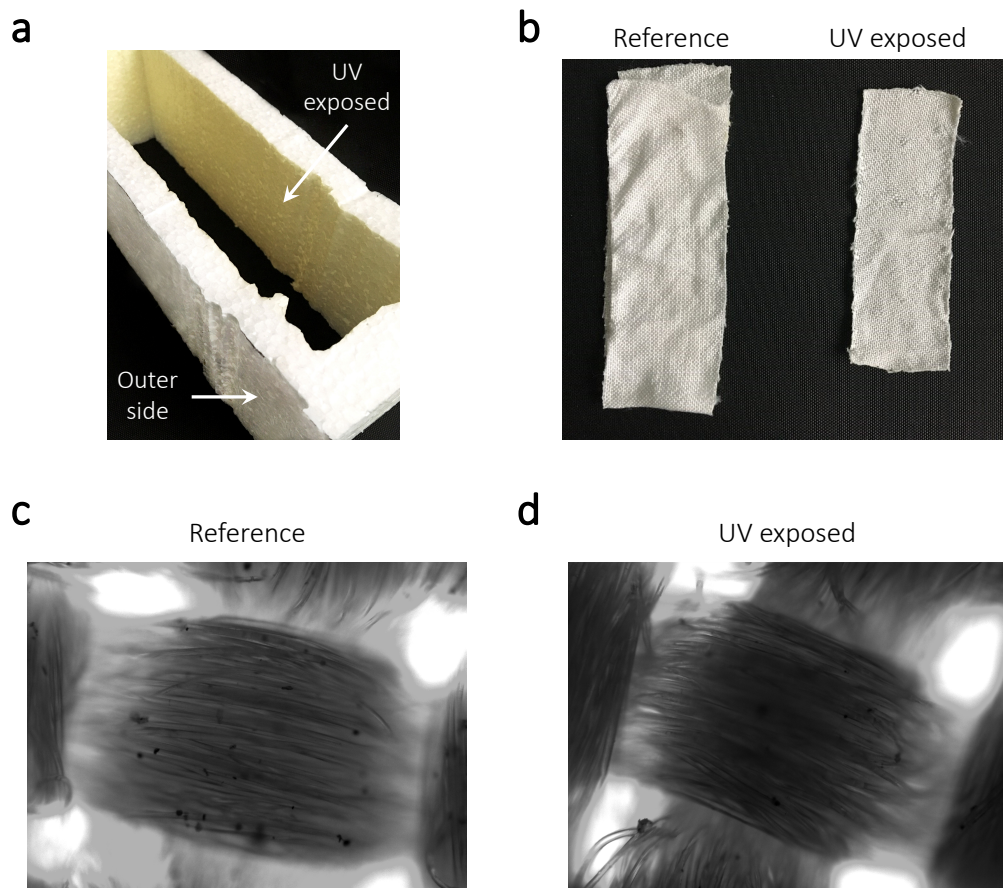
Supplementary Figure 13: Durability and the hydrophilicity restoration of the PE fabric under UV light exposure. (a) A photo of the setup used for the fabric UV exposure testing. (b) Optical photographs of the woven PE fabric samples before and after 2 weeks of UV exposure. (c,d) Optical microscopy images of the woven PE fabric samples before (c) and after 2 weeks of UV exposure (d).

After exposure to UV light, the hydrophilicity of the textile was evaluated by depositing water droplets on the sample, which was folded to avoid interaction with the support, and observing their penetration. While the reference sample could not wick water, the droplets penetrated the UV-exposed textile (see Supplementary Video 4). This suggests that hydrophilicity of the PE fibers and textiles can be restored by regular exposure to sunlight.

We also observed experimentally that mechanical friction – a process that naturally occurs in the process of fabrics wearing, washing, and tumble-drying – easily restores the PE fabrics hydrophilicity (see Supplementary Video 3). As a perspective, charged particles might be encapsulated in the PE fibers during the fabrication, increasing the hydrophilicity by their electric field without being washed away by the flowing water. However, this will require further studies, which can be the subject of a separate follow-up publication.

10. Microscopic permeability of the yarn along the fiber axis

The porosity of the periodic hexagonal-lattice and the square-lattice yarns, namely the ratio between the void and the total area within a representative volume element, can be related to the fiber radius and the inter-fiber separation by geometrical considerations as:

$$\phi_H = 1 - \frac{\pi}{2\sqrt{3}\left(1+\dfrac{d}{r}\right)^2} \; , \tag{16}$$

$$\phi_S = 1 - \frac{\pi}{4\left(1+\dfrac{d}{r}\right)^2} \; . \tag{17}$$

Here, r is the fiber radius, $2d$ is the surface-to-surface distance between adjacent fibers (see Supplementary Fig. 14b), and the subscripts H and S refer to the hexagonal and square lattices, respectively.

The microscopic permeability K of unidirectional fibrous media in the direction of the fibers axis is a function of the fiber radius, the yarn porosity, and the lattice structure, and can be computed as[24,25]:

$$K = r^2 \exp\frac{\left(B + C(1-\phi)\right)}{(1-\phi)^m} \; , \tag{18}$$

where the parameters

$$B = 5.43 - 18.5(1 - \phi_{min}) + 10.7(1 - \phi_{min})^2 \; , \tag{19}$$

$$C = -4.27 + 6.16(1 - \phi_{min}) - 7.1(1 - \phi_{min})^2, \tag{20}$$

$$m = -1.74 + 7.46(1 - \phi_{min}) - 3.72(1 - \phi_{min})^2 \tag{21}$$

depend on the minimum porosity ϕ_{min} that can be achieved in a specific lattice structure under the densest packing scenario. The above model for the microscopic permeability has been previously validated against finite element simulations in the porosity range $0.1 \div 0.9$[24,25]. The minimum porosity of both types of the fiber arrangements corresponds to the situation when the adjacent fibers are in direct contact, namely $d = 0$, which leads to $\phi_{H,min} = 9.3\%$ and $\phi_{S,min} = 21.5\%$.

11. Modelling of the capillary pressure in an ideal yarn

The capillary pressure $p_c = \rho g h_{max}$ is a function of the fluid density ρ, the gravitational acceleration g and the maximum capillary height h_{max}, which in turn is a function of the yarn porosity, the fiber radius and the water-fiber contact angle. In this work, the maximum capillary rise was computed according to the model proposed by Princen[26,27].

The correct method to evaluate h_{max} depends on the yarn porosity. At $\phi = \phi_{min}$, the contact between adjacent fibers leads to an asymptotically infinite capillary rise. For $\phi > \phi_{min}$, two types of menisci form in the system: a higher water column between each pair of adjacent fibers, and a lower one in the channel formed by each triplet or quadruplet of fibers in the unit cell of a periodic lattice (Supplementary Fig. 14a,b). The equations required to compute the height of the two menisci are described in Supplementary Note 11.1. With the increase of the yarn porosity, the higher water column is reduced more than the lower one, until they join at the critical value of porosity ϕ_{cr} (see Supplementary Note 11.2). Finally, ϕ_{max} is the maximum value of the porosity for which the capillary rise still takes place, which depends on the fiber-water contact angle θ, the number of fibers in the yarn, and their arrangement. The method used to evaluate ϕ_{max} is

reported in Supplementary Note 11.3. The model was used to explore the influence of the parameters on the dynamic wicking of an ideal yarn when $\phi_{cr} < \phi < \phi_{max}$ (see Supplementary Note 11.4 and the main text), under the assumption that the maximum capillary height is larger than the height of the meniscus, approximated as the fiber radius, namely $h_{max} \gg r$.
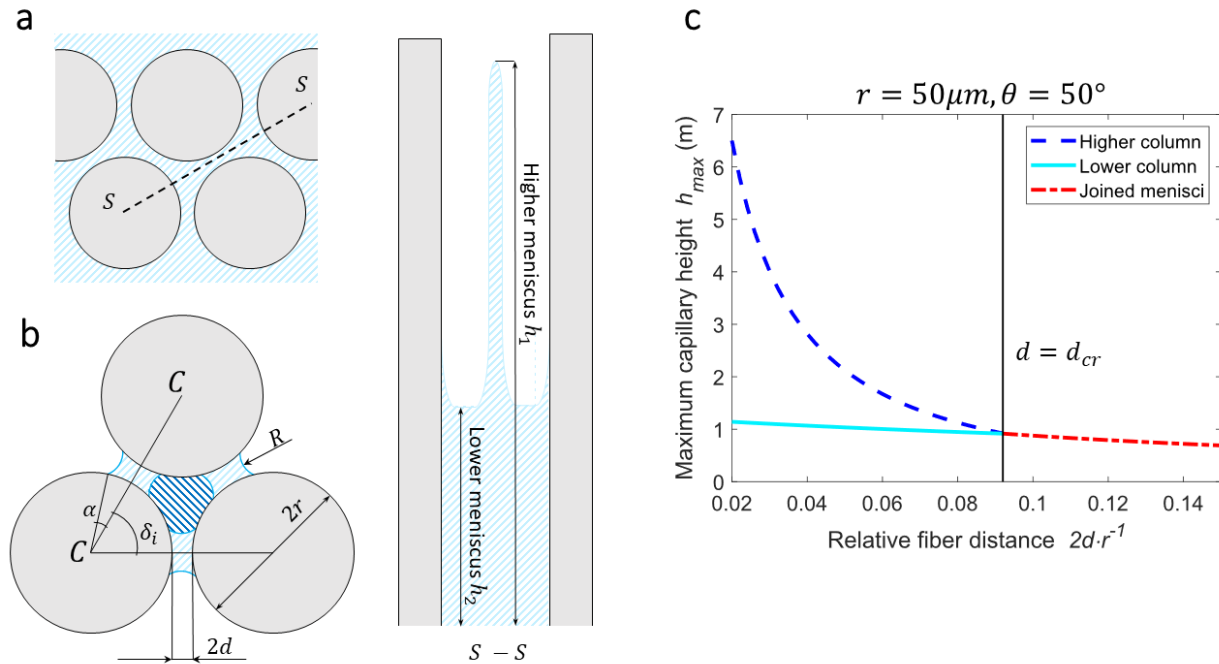
Supplementary Figure 14: Theoretical modelling of the capillary suction in a periodic infinite array of parallel fibers with a hexagonal symmetry. (a) Sketch representing the two menisci formed in the system when the yarn porosity is $\phi < \phi_{cr}$. (b) Schematics of the water columns formed in a three-fiber system. The higher meniscus forms between each pair of adjacent fibers (light-blue shaded area), while the lower meniscus forms in the channel created by each triplet of fibers (dark-blue shaded area). (c) Dependence of the maximum height of the water columns on the relative fibers separation $2d \cdot r^{-1}$. The height of the higher meniscus decreases faster than the other one, until they merge at $d = d_{cr}$. The depicted results are obtained for $r = 50\,\mu m$ and $\theta = 50°$.

11.1. Capillary interaction in a multi-fiber infinite yarn for $\phi_{min} < \phi < \phi_{cr}$

When $\phi < \phi_{cr}$, the water-fiber interaction leads to the formation of two types of menisci, as sketched in Supplementary Fig. 14a,b. The higher one forms between each pair of adjacent fibers (light blue dashed area), the lower one forms in the channel created by each triplet of fibers (dark blue dashed area). The heights of the two menisci, respectively h_1 and h_2, can be computed considering the corresponding force balance between the vertical component of the surface tension and the weight of the water column subtended to each meniscus:

$$F_i = h_i \rho g A_i \,, \tag{22}$$

where A_i is the cross-section of the water column sustained by the capillary force F_i. Until the end of the current section, the subscripts "1" and "2" are used to refer the height-dependent parameters to h_1 and h_2, respectively.

The cross section of the water column subtended each higher meniscus (the light blue shaded areas of Supplementary Fig. 14b) can be computed as:

$$A_1 = 2r^2 \left\{ \frac{2R_1}{r} \sin(\alpha_1)\cos(\theta + \alpha_1) - \alpha_1 + \sin(\alpha_1)\cos(\alpha_1) \right.$$
$$\left. - \left(\frac{R_1}{r}\right)^2 \left[\frac{\pi}{2} - \theta - \alpha_1 - \sin(\theta + \alpha_1)\cos(\theta + \alpha_1)\right] \right\}, \tag{23}$$

where R is the external radius of curvature of the water column, r is the fiber radius, and α is the angle between the line connecting the centers of two adjacent fibers $C - C$ and the radius connecting the center of a fiber to the triple-contact line of the water meniscus. The curvature radius R can be geometrically computed as:

$$\frac{R_i}{r} = \frac{1 + \frac{d}{r} - \cos(\alpha_i)}{\cos(\theta + \alpha_i)} . \tag{24}$$

The capillary force consists of two contributions: a component directed upwards due to the water-fiber interaction $F_{1,up}$, and a component directed downwards due to the water-air interaction $F_{1,dw}$. The two components can be respectively expressed as:

$$F_{1,up} = 4\gamma r \alpha_1 \cos\theta, \qquad F_{1,dw} = -4\gamma \left(\frac{\pi}{2} - \theta - \alpha_1\right) R_1, \tag{25}$$

here γ is the water surface tension. Re-arranging the former equations, a quadratic equation is obtained, which can be iteratively solved for a given fiber separation d to obtain the corresponding maximum height of the higher meniscus from the equilibrium between the Laplace's and the hydrostatic pressure:

$$h = \gamma/\rho g R . \tag{26}$$

The height of the lower meniscus can be calculated similarly to the previous case, by balancing the water-fiber capillary force, only directed upwards, and the weight of the water column subtended to the meniscus (dark blue shaded area in Supplementary Figure 14b). The cross-section of the water column at the height h_2 can be computed as[27]:

$$A_2 = 3r^2 \left\{ \left(\frac{R_2}{r}\right)^2 \left[\frac{\cos^2(\theta + \alpha_2)}{\sqrt{3}} + \frac{\pi}{2} - \theta - \alpha_2 - \sin(\theta + \alpha_2)\cos(\theta + \alpha_2)\right] \right.$$
$$+ \frac{R_2}{r}\left[\frac{2\cos(\theta + \alpha_2)\cos(\alpha_2)}{\sqrt{3}} - 2\sin(\alpha_2)\cos(\theta + \alpha_2)\right]$$
$$\left. + \frac{\cos^2(\alpha_2)}{\sqrt{3}} + \alpha_2 - \frac{\pi}{6} - \sin(\alpha_2)\cos(\alpha_2)\right\}, \tag{27}$$

while the upward capillary force can be computed as:

$$F_{1,up} = 3\gamma r \left[2\left(\frac{\pi}{2} - \alpha_2 - \theta\right)\frac{R_2}{r} + \left(\frac{\pi}{3} - 2\alpha_3\right)\cos\theta\right]. \tag{28}$$

Combining the previous equations, another quadratic form can be obtained, which can be solved for a separation d to compute the corresponding maximum height h_2 from Supplementary Eq. 26. The maximum heights of the two menisci for different values of the relative fibers distance $2d \cdot$

r^{-1} are plotted in Supplementary Fig. 14c for a bundle of fibers with $r = 50 \, \mu m$ and $\theta = 50°$, arranged in a hexagonal structure.

11.2. Capillary interaction in a multi-fiber infinite yarn for $\phi_{cr} \leq \phi < \phi_{max}$

Given the large number of fibers in the yarn tested in this work ($n_f = 247$), the maximum capillary height h_{max} is computed considering the yarn as composed by an infinite number of fibers, namely $n_f \to \infty$ [26]. With this assumption, the water menisci at the boundary between each computational cell and its neighbors can be considered flat in the plane perpendicular to the fiber axis, and the downward force acting on the water column at the boundary of the yarn can be neglected. Thus, at the equilibrium, h_{max} can be computed considering the force balance between the vertical component of the surface tension at the water-fiber interface and the weight of the water column [26,27]. The force balance can be expressed as:

$$F_c = h_{max}\rho g A ,$$
(29)

where A is the lattice-dependent cross-section of the liquid column, ρ is the water density, g is the gravitational acceleration, and F_c is the capillary force, expressed as:

$$F_c = \gamma P \cos \theta .$$
(30)

Here, γ is the wetting fluid surface tension, P is the wetted perimeter, and θ is the liquid-fiber contact angle. Considering the hexagonal and square fiber arrangements, it holds:

$$P_H = 6\pi r , \qquad P_S = 2\pi r,$$
(31)

$$A_H = r^2\big(6\sqrt{3}(1 + d/r)^2 - 3\pi\big), \qquad A_S = r^2(4(1 + d/r)^2 - \pi).$$
(32)

Thus, the above equations can be re-arranged to obtain the maximum capillary height for both lattice symmetries:

$$h_{max} = \frac{2 \cos \theta \, (1 - \phi)}{rc^2\phi} ,$$
(33)

where $c^2 = \rho g/\gamma$. As it can be seen, h_{max} only depends on the fiber radius r, contact angle θ and yarn porosity ϕ, justifying their choice as the design parameters.

11.3. Evaluation of the maximum porosity ϕ_{max} of a finite-size ideal yarn

The maximum porosity ϕ_{max}, namely the maximum porosity for which the capillary rise still takes place, can be computed from the force balance between the upward capillary force acting on the perimeter of the wet fibers, and the downward component of the air-water surface tension acting on the water column at the outer boundary of the yarn. The vertical liquid column presents a single, height-dependent curvature radius R, which determines the maximum capillary height from Supplementary Eq. 26.

Defining α as the angle between the line connecting the centers of two adjacent fibers and the radius connecting the center of a fiber to the triple-contact line of the water meniscus (see Supplementary Fig. 14b), when $\alpha + \theta = \pi/2$, the curvature radius $R \to \infty$ and no capillary rise

can take place. Therefore, the force does not depend on the weight of the water meniscus, and the following condition holds:

$$P_{wf} \gamma \cos\theta - P_{aw}\gamma = 0 , \tag{34}$$

where P_{wf} is the wet perimeter of the fibers and P_{aw} is the perimeter of the air-water contact line in the plane perpendicular to the fiber axes. At the limit of null capillary suction $\alpha + \theta = \pi/2$ and $R \to \infty$, the above equation can be rewritten as:

$$\left(\sum_{i=1}^{n_{fB}} R\left(\delta_i + 2\left(\frac{\pi}{2} - \theta\right)\right) + 2\pi R \cdot n_{fD} \right) \cos\theta - n_{fB} \tag{35}$$

$$\cdot\, 2R\left(1 - \sin\theta + \left(\frac{d}{R}\right)_{max}\right) = 0 ,$$

where n_{fB} is the number of fibers on the boundary of the yarn, n_{fD} is the number of fibers completely surrounded by water, and δ_i the the angle between the lines connecting the center of the i-th fiber at the yarn boundary with the center of its neighboring boundary fibers (see Supplementary Fig. 14a,b). For the hexagonal arrangement, four values of δ_i are possible: $\pi/3$, $2\pi/3$, π and $4\pi/3$; while for the square arrangement the possible configurations of δ_i are: $\pi/2$, π and $3\pi/2$.

Under the assumption of $n_f \to \infty$, the ratio $n_{fD}/n_{fB} \to 0$ and Supplementary Eqs. 16-17 and 35 lead to $\phi_{max} \to 1$, meaning that even infinitely distant fibers produce a relevant capillary suction, which is clearly non-physical. To overcome this limit and provide a more reliable estimation of the maximum fibers distance allowed to promote capillary suction, we developed a growth model of an ideal yarn, which automatically computes n_{fD}, n_{fB} and δ_i for a given n_f and fiber arrangement. The resulting ideal, finite-size yarn is supposed to be composed of concentric layers of fibers, starting from a central core unit, and added one by one to maintain at best the circular shape of its border. A MATLAB routine is implemented to perform the computation for $n_{tot} = n_{fB} + n_{fD} > 13$ and $n_{tot} > 4$ for the hexagonal and square arrangement, respectively.

effect of the uncertainty of the contact angle.

Supplementary Fig. 15 shows the dependence of the maximum relative fiber distance $(2d/r)_{max}$ on n_f and θ. The parameter $(2d/r)_{max}$ is computed from Supplementary Eq. 35 and is used to evaluate ϕ_{max} through Supplementary Eqs. 16 and 17 for the hexagonal and square fibers arrangement, respectively. The green hexagram shows $(2d/r)_{max}$ when the proposed growth model is used, considering $n_f = 247$ and $\theta = 71.3°$. This ideal result is compared with the actual yarn structure (red circle), evaluated for the same value of θ, while n_{fB} and n_{fD} were counted from 11 yarn cross-sections images obtained via micro-CT, where $\sum_i^{n_{fB}} \delta_i = 2\pi/3 \cdot (n_{fB}/2) + 4\pi/3 \cdot (n_{fB}/2)$ for the hexagonal structure, $\sum_i^{n_{fB}} \delta_i = 2\pi + \pi/2 \cdot (n_{fB} - 4)$ for the square structure. The uncertainty on the experimental value of the contact angle was used to compute a maximum and minimum value of ϕ_{max} for each configuration. Finally, the results were averaged, and the error bars were evaluated considering the dispersion of the data.
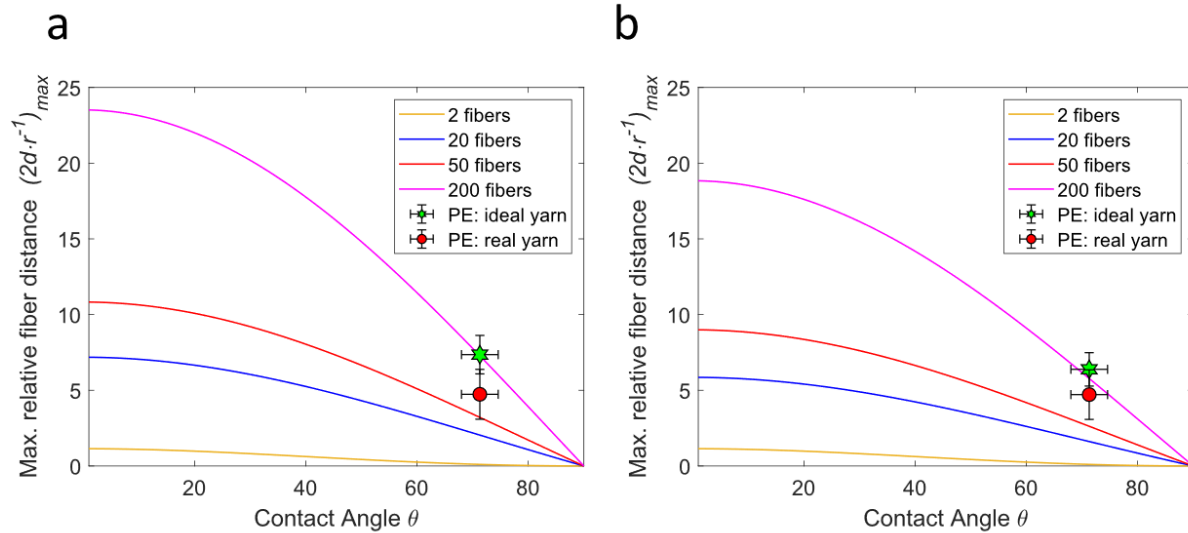
Supplementary Figure 15: Maximum fiber distance in a finite-size yarn. The maximum porosity ϕ_{max} for hexagonal (a) and square (b) fiber arrangement was expressed in terms of the maximum relative fiber distance $(2d/r)_{max}$, computed with Supplementary Eq. 35. This parameter can be used to retrieve ϕ_{max} through Supplementary Eqs. 16-17. The lines show the model predictions for ideal yarns with different number of hexagonal- or square-arranged fibers. Intuitively, lower values of θ allow wicking with lower fiber packing density, while increasing the number of fibers yields capillary suction with less hydrophilic fibers. The green star shows the model predictions for the ideal yarn, computed with the growth model proposed, considering $n_f = 247$ and $\theta = 71.3°$. The reported error bars were evaluated considering the effect of the uncertainty of the measured contact angle on the resulting value of $(2d/r)_{max}$. The red circle shows the maximum relative fiber distance for a real yarn, considering the same θ, while n_{fB} and n_{fD} were obtained from micro-CT scans.
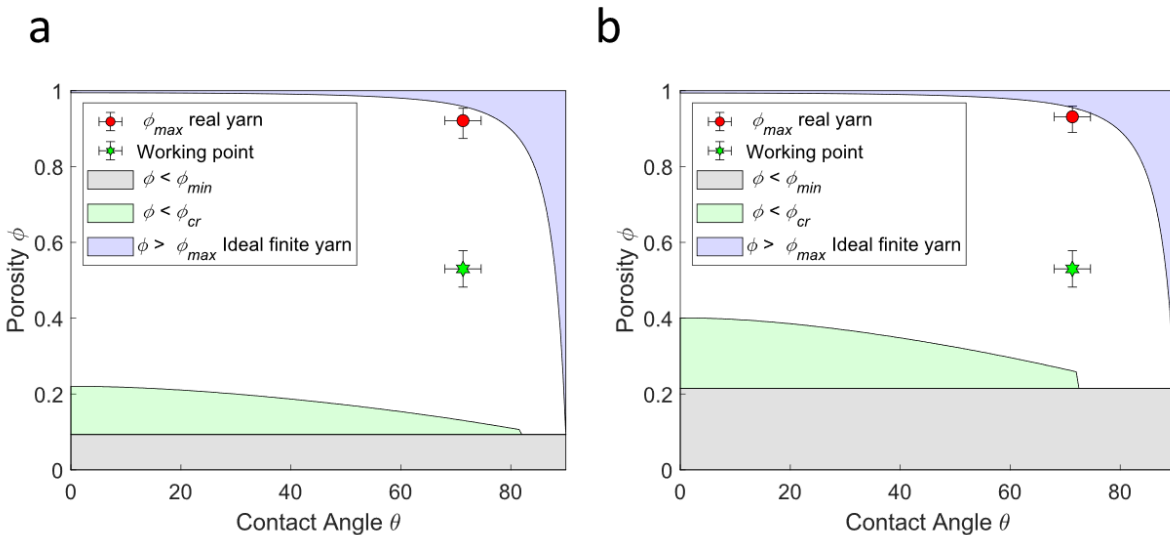
Supplementary Figure 16: Limits of the model for simulating the yarn composed of 247 fibers with the values of fiber radii extracted from the experimental data. Domain of validity of the theoretical model used to predict the wicking properties of the woven PE textile for (a) hexagonal and (b) square fibers arrangements. The working point and its error bars are evaluated considering the experimental data obtained from the characterization of the PE fibers, namely $\theta = (71.3 \pm 3.3)$ ° and $\phi = (53.0 \pm 4.8)$ %. ϕ_{max} of the real yarn (red dot) is computed according to the methodology described in Supplementary Note 11.3.

Supplementary Fig. 16 shows the domain of the model validity (white area) for a yarn composed of 247 fibers, with the fibers diameter obtained from the experimental measurements of the woven PE yarns. The red circle shows the maximum yarn porosity ϕ_{max} (within experimental uncertainty) computed from Supplementary Eq. 35 for $\theta = (71.3 \pm 3.3)$ °, while n_{fB} and n_{fD} were evaluated from the yarn cross-sections images, as previously described. The green hexagram corresponds to the combination of parameters of the real PE yarn used in this work: $\theta = (71.3 \pm 3.3)$ ° and $\phi = (53.0 \pm 4.8)$ %. Since both the hexagonal and square fiber arrangements fall within the white area, it possible to approximate the maximum capillary height h_{max} with Supplementary Eq. 33.

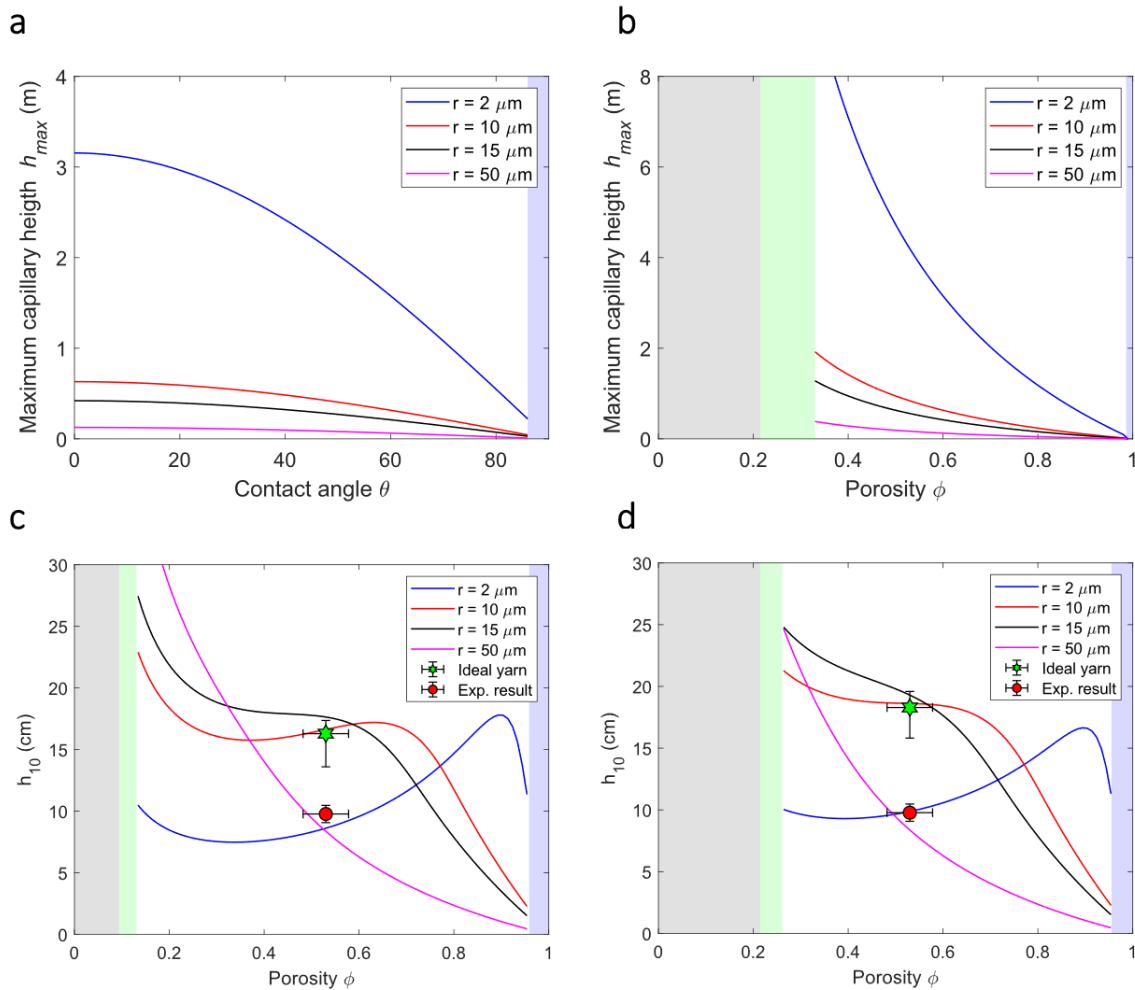## 11.4. Model predictions of the wicking performances of an infinite ideal yarn with $\phi_{cr} \leq \phi < \phi_{max}$

The model described in detail in Supplementary Notes 11.1-11.3 has been used to explain the results of the wicking experiments for the woven PE textile and to predict the optimum yarn configuration to maximize the fabric wicking performance. Supplementary Figs. 17a,b show the effects of the water-fiber contact angle θ and of the yarn porosity ϕ on the maximum height of the water front h_{max}, computed with Supplementary Eq. 33 for different values of the fiber radii. The results shown in Supplementary Fig. 17a,b are produced for the square arrangement of fibers, but similar conclusions can be drawn for the hexagonal structure. The data show that the capillary pressure increases when the yarn is composed by small, hydrophilic and densely packed fibers, yielding larger values of h_{max}. However, this combination of parameters may not yield the optimized wicking properties of the system, which can be expressed by the highest point reached by the water front after a given imbibition time h_t.

Supplementary Figs. 17c,d illustrate the effect of the yarn porosity and the fiber radius on the height reached by the water front after 10 minutes of imbibition (i.e. h_{10}), for a hexagonal (panel c) or square (panel d) arrangements of fibers with a contact angle of $\theta = 71.3°$, as experimentally characterized (see Eqs. 1-3 in Methods for the details on the time-dependent model). The color shaded areas are used to represent the domain of applicability of the model. The plots show the predicted performances of the woven PE textile, computed considering the measured average fiber diameter $2r = 18.5 \, \mu m$ and a yarn porosity of $\phi = 53$ %, in the limit of infinite-size periodic-lattice yarn. As it can be seen, the performance of the ideal textile depends non-linearly on r and ϕ.

The data in the Supplementary Figs. 17c,d show that depending on the yarn symmetry and the average fiber diameter, the optimal wicking properties of the yarn are achieved at different porosity values. The value of h_{10} for each yarn configuration is determined by two competing phenomena: the capillary pressure, which is a function of the maximum capillary height ($p_C = \rho g h_{max}$), and the viscous friction between water and the fibers, which is a function of the microscopic permeability K along the fibers axis. h_{10} increases with the increase of either p_c and K. As shown in Supplementary Figs. 17a,b, the capillary pressure increases when the yarn is composed of small, hydrophilic and densely packed fibers. On the other hand, K increases in yarns composed of large and widely-separated fibers, as the resistance to the water motion decreases[24]. As a result, yarns composed of small fibers present better overall wicking properties for large values of ϕ, while low-porosity yarns are favored when larger fibers are used.

Finally, Fig. 2g in the main text and Supplementary Fig. 18 show the 3D plots illustrating the dependence of h_{10} on both the yarn porosity and the individual fiber diameter for the fiber contact angle of 71.3^o for the square fiber arrangement (Fig. 2g) and the hexagonal fiber arrangement (Supplementary Fig. 18). These plots can be used to optimize the yarn structure for the optimum wicking performance.

Supplementary Figure 17: Theoretical predictions of the woven PE textile wicking performance. (a-b) Maximum capillary height h_{max} in a square-symmetry yarn as a function of the contact angle (a) and the yarn porosity (b) for different fiber radii computed with Supplementary Eq. 33. The two plots are obtained considering $\phi = 0.5$ (a) and $\theta = 50°$ (b), respectively. The color-shaded areas highlight the upper and lower bounds of validity of the proposed model: $\phi < \phi_{min}$ (gray), $\phi < \phi_{cr}$ (green) and $\phi > \phi_{max}$ (blue). (c-d) Theoretical prediction of the water column height after 10 minutes of vertical imbibition (h_{10}) for $\theta = 71.3°$ considering a hexagonal (c) or square (d) fiber arrangement and different fiber radii. The green hexagon reports h_{10} for an infinite ideal yarn composed of fibers with diameters of $(18.5 \pm 6.2) \, \mu m$, contact angles of $71.3 \pm 3.3°$, with porosity of $(53.0 \pm 4.8)\%$. The red circles correspond to the experimentally measured h_{10} value for the woven PE textile.

Alternatively, 3-dimensional fluid dynamics simulations can be used to evaluate the effect of the shape and arrangement of the fibers on the average capillary properties of the textile, namely the permeability $\mathbf{K}$ and the capillary pressure $\mathbf{p_c}$. While it is outside of the scope of the current paper, this analysis will be used in the follow-up work to optimize the knitting/woven patterns of the PE fabrics for efficient moisture transport.
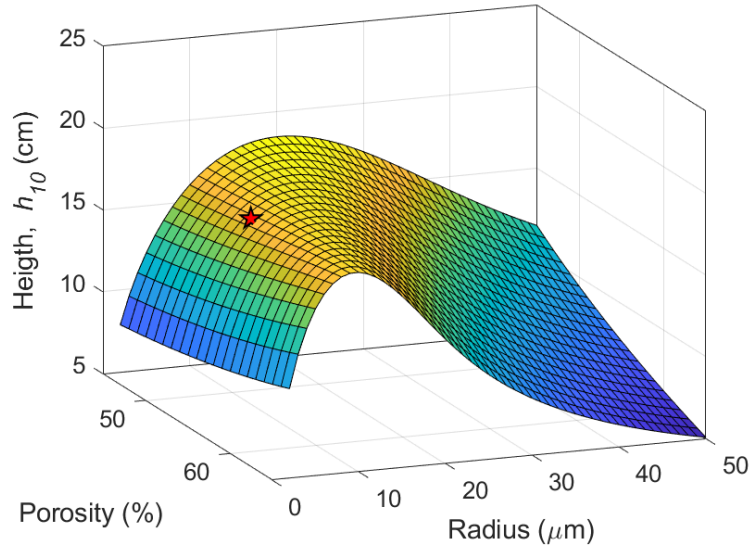
Supplementary Figure 18: Fabric structure optimization to achieve efficient wicking. The height of the wet area in the ideal hexagonal-lattice PE yarn 10 mins after exposure as a function of the fiber radius and the yarn porosity for a fixed contact angle of 71.3°. The red star represents the performance of an ideal yarn with the same parameters as the PE multi-filament yarn used in this work.

## 12. Drying rate and evaporative cooling performance of fabrics

The drying properties of the fabrics were measured via the ISO 17617 standard (method B). The circular fabric test specimens (85 ± 2) mm in diameter were kept at the room temperature and relative humidity of (40 ± 5) %, measured with a hygrometer (RH820, Omega instruments), for one day. The ambient temperature was monitored with a thermistor (model 4033, Omega instruments) and maintained at (23.6 ± 0.3) °C. Each sample was laid in a Petri dish placed on a precision balance (Mettler Toledo, NewClassic ML), weighed and removed. Then, (0.25 ± 0.02) ml of distilled water was applied using a micropipette to the center of the base of the Petri dish and covered by the test fabric specimen. The whole setup was exposed to the environment (Fig. 3a,b), and the ambient temperature and humidity were measured during the experiment. The weight loss caused by water evaporation was measured for 2 hours. With these data, the drying time and drying rate (% per minute) were calculated using the least squares fitting method (Supplementary Table 3).

Supplementary Table 3: Drying rate and drying times of the textiles. The drying time of each sample is evaluated as the time when the residual mass of the water falls below 1% of the dry sample mass $(m_{end} - m_0)/m_0 \leq 1\%$.

Materials	Drying rate (%/min)	100% drying time (min)
Cotton	2.1 ± 0.1	48.9
Linen	1.4 ± 0.1	76.9
Polyester	3.0 ± 0.2	34.3
Tyvek	1.7 ± 0.1	58.0
Woven PE	3.5 ± 0.3	29.4

To evaluate the effect of the evaporation on the spatial temperature distribution, the evaporation tests were repeated by substituting the Petri dish with a polystyrene plate 10x10 cm wide and 2

cm thick. A thermistor (model 4033, Omega instruments) was placed at the center of the specimen surface. Three other thermistors were positioned in radial direction from the central one with an equal spacing of 1 cm (Fig. 3e) and covered with a water-resistant tape, to prevent the direct contact between the distilled water and the sensing elements. The distilled water basin was kept on a heated magnetic stirrer to maintain the temperature difference between the reservoir, measured with a properly insulated thermistor, and the average temperature of the plate surface within 0.2°C. The micropipette was kept immersed in the reservoir to achieve thermal equilibrium with water. All the data from the thermistors were acquired with a digital data logger (OM-CP-OCTPRO, Omega instruments) using a sampling frequency of 1 sample/s.
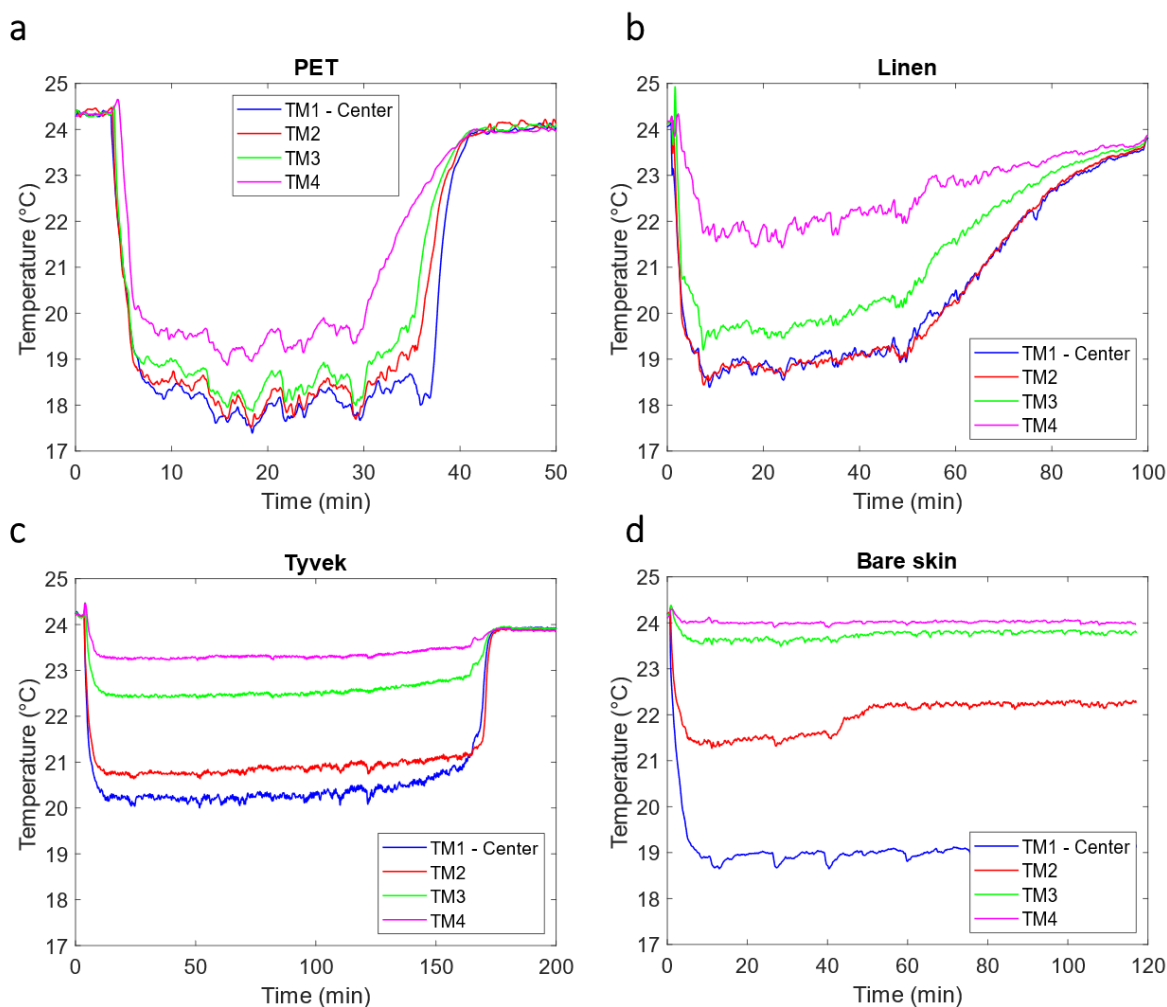
Supplementary Figure 19: Temperature distributions during the evaporation tests. The temperature data recorded by the four thermistors as a function of time after the droplet was deposited and the 'skin' covered with (a) woven polyester (PET) fabric, (b) woven linen fabric, (c) non-woven Tyvek PE textile. (d) Reference temperature data for the bare 'skin' covered by the droplet at the center. The different wicking properties of the materials tested result in different temperature distributions over the artificial 'skin' covered by each textile.

The temperature data quantifying evaporative cooling performance of the woven PE and woven cotton textiles are shown in Figs. 3f,i. Supplementary Fig. 19 summarizes the corresponding data for woven polyester (PET) (panel a), woven linen (panel b), non-woven Tyvek PE material (panel c), and bare surface ('skin') (panel d).

Polyester (a) and woven PE fabrics (see Fig. 3f) exhibited rapid wet-to-dry transitions owing to the hydrophobicity of their fibers cores. On the other hand, linen (b) and cotton (see Fig. 3g) are composed of microporous, hydrophilic fibers absorbing water, which reduces the effective evaporation area. When Tyvek (c) was used, the evaporation rate was reduced by its hydrophobic properties, which hinders the diffusion of water vapor and does not allow an effective spread of the water droplet. As a reference (d), a water droplet was placed at the center of the 'skin' and was allowed to evaporate without being covered with any textile. The effects of evaporative cooling in different textiles can be easily appreciated, reflected in similar values of minimum temperature achieved at the droplet deposition site (TM1, blue line), but very different temperature distributions and wet-to-dry transitions. Overall, the woven PE fabric exhibited the fastest temperature drop and recovery, and the most uniform temperature distribution on all the four thermistors, indicative of the efficient moisture lateral spreading and evaporation processes.

The drying tests were repeated for the three fabrics presenting the highest evaporation rates, namely woven PE, woven polyester (PET) and woven cotton textiles. The results are shown in Supplementary Fig. 20 and are comparable with those presented in Fig. 3 and Supplementary Fig. 19. Among the materials tested, the woven PE dried the fastest, while cotton had the lowest evaporation rate, which was hindered by the absorption of water within its porous fibers.
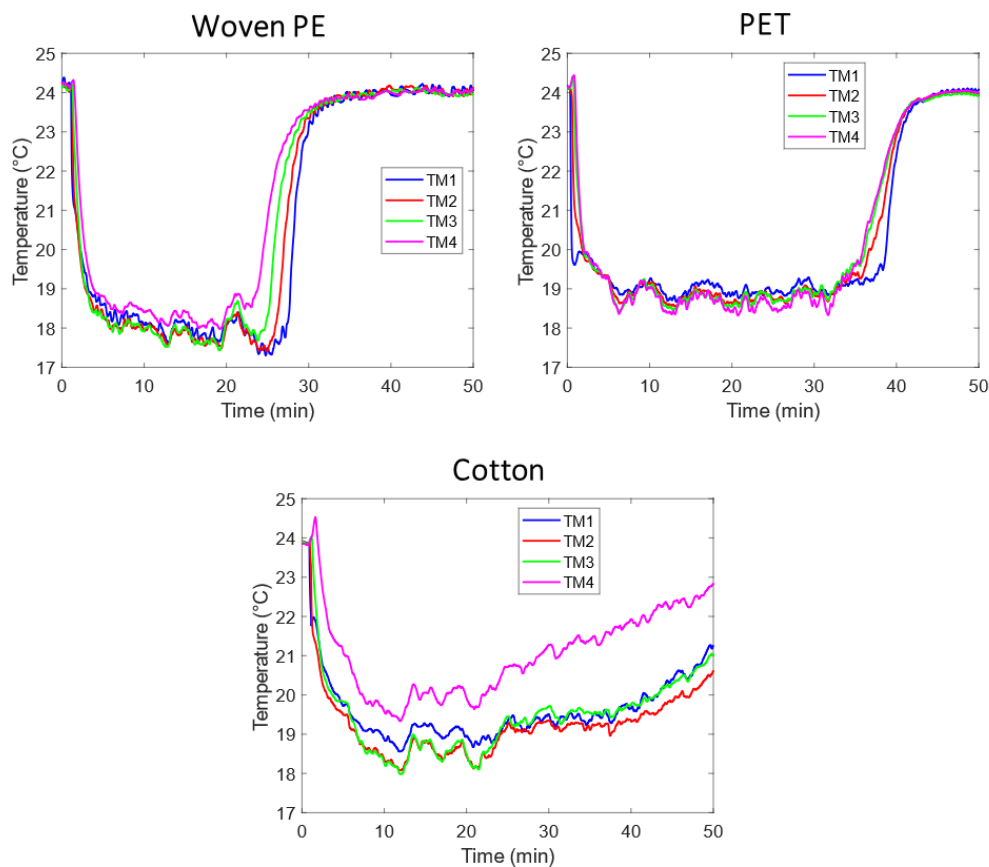
Supplementary Figure 20. Temperature distributions during the evaporation tests; reseated experiments for woven PE, cotton, and polyester (PET). These results are comparable with those presented in Supplementary Fig. 19.

The times-to-dry obtained from the measurements are reported in the Supplementary Table 4 below. The three tests reported were performed the same day and stable ambient conditions: the expanded uncertainty of the ambient temperature and the relative humidity are respectively 0.3 °C and 5%. We want to point out that the drying tests performed aim to be comparative, thus evaluating which material dries faster at given ambient conditions, rather than providing general drying performances.

Supplementary Table 4: Drying times of the textiles in a repeated test.

Material	100% drying time [min]
Woven PE	28
PET	39
Cotton	55

13. Principal Component Analysis (PCA) of the near-infrared spectra of fibers

Both, natural and synthetic fibers and fabrics are composed of macromolecular polymers. Polymer macromolecules typically contain C, H, O, and N atoms, which are arranged in repeating groups in various combinations (see Figs. 4a-c). Interaction of infrared radiation with polymers results in frequency-selective light absorption when the frequency of radiation coincides with the vibrational frequencies of these atomic groups. The resulting absorption bands in the material infrared spectrum always appear at the same wavelength position, and can serve as molecular "fingerprints" to identify and sort different polymers.

The fundamental vibrational modes include stretching of chemical bonds, in-plane and out-of-plane deformations, wagging, twisting, and rocking. While the fundamental stretching modes of CH bonds center around the mid-infrared wavelength of 3.4 micron, the overtones and combination bands of fundamental vibrational modes have characteristic wavelengths in the near-infrared spectral range (between 1 and 2.5 micron). Owing to the availability of low-cost light sources and photo-detectors in this spectral range, near-IR vibrational bands are typically used as molecular fingerprints to separate polymers via the automated sorting and recycling processes.

The near-IR vibrational bands are comprised of the overtones of stretching vibrations of groups containing hydrogen, as well as of combinations of these stretching vibrations with wagging and/or rocking vibrations. The characteristic resonant wavelengths of the first and second overtones of the CH stretching mode are centered around 1.7 micron and 1.2 micron, respectively. The presence of other atomic groups (e.g., aromatic CC bonds) in the macromolecule chain may modify the characteristic wavelengths of the CH bonds, providing additional information to distinguish between different polymers by analyzing their near-IR spectra. The resonant frequencies of combination bands lie between the fundamental vibrations and various overtone modes. Some functional hydrogen-free atomic groups also exhibit strong near-IR absorption, such as e.g., CO bands appearing in the $1900 - 2000$ nm wavelength range in the infrared spectra of polyester and other synthetic polymers.

However, garments and textiles often contain dyes, pigments, plasticizers, and other additives such as flame retardants, UV stabilizers, and chemical coatings to improve fiber hydrophilicity or

hydrophobicity. These materials have their own characteristic spectral fingerprints due to light absorption via both vibrational modes activation and electronic transitions, which can obscure the polymer fingerprints and prevent automated recycling. Dark-colored textiles and plastics are often rendered non-recyclable and either go straight to landfill or are incinerated, because the strong absorption in the colorants across both visible and near-infrared spectral ranges prevents spectral identification of polymers.
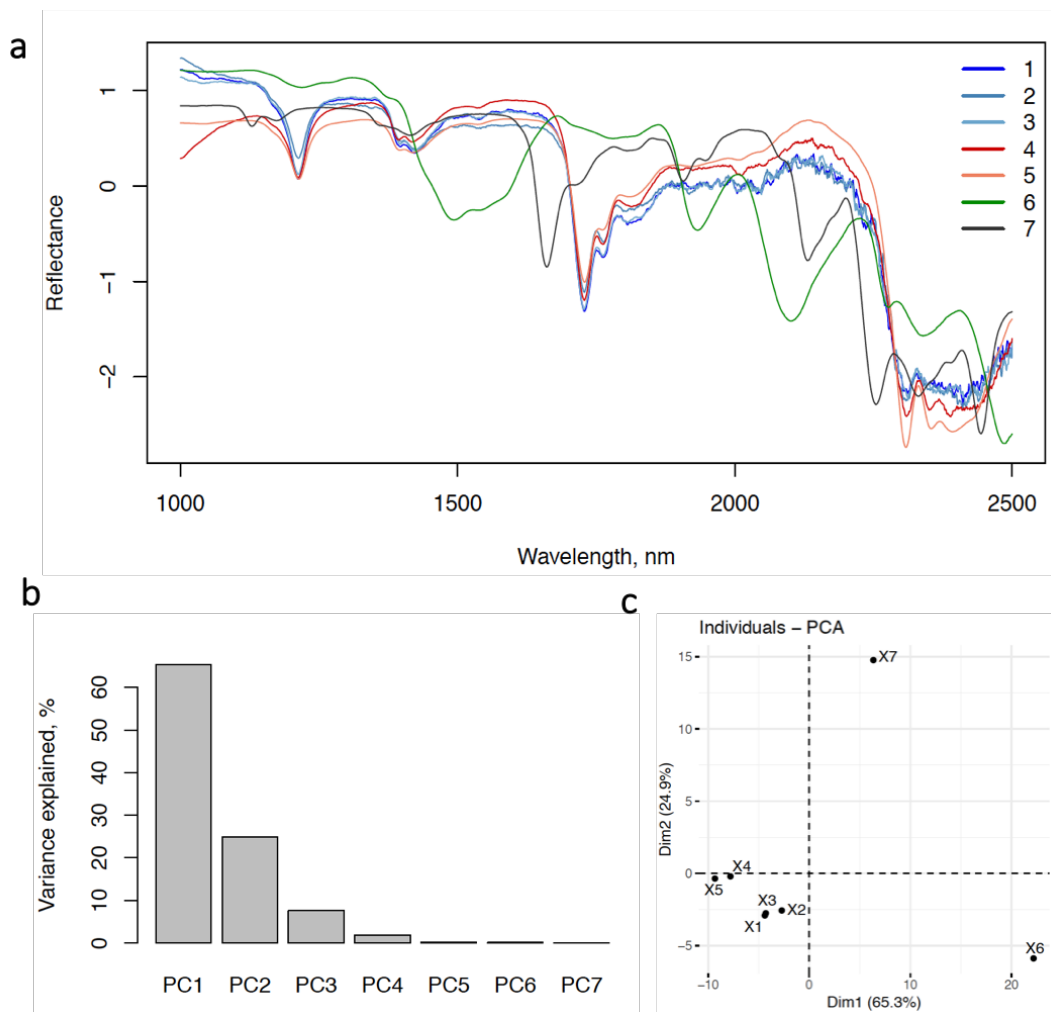
Supplementary Figure 21: Principal component analysis (PCA) of the near-infrared spectra of different polymer fibers and textiles. (a) Reflectance spectra from Fig. 5b, re-normalized as z-scores for the PCA analysis. (b) The contributions to the spectral variance from different principal components. (c) The PCA scatter plot with PC1 and PC2 components used as axes.

The spin-dyeing process adopted for coloring PE fibers and textiles allows using a wide variety of non-traditional colorants, which can be chosen such that they do not obscure the near-IR spectral fingerprints of the polyethylene macro-molecule. To confirm that colored PE fibers can still be distinguished clearly from other polymer fibers and textiles, we used the principal component analysis (PCA)[28] to identify the main sources of variation in the infrared spectra of LLDPE and HDPE fibers with and without colorants and in the corresponding spectra of cotton and polyester textiles. The near-IR spectra of different fibers and fabrics (Fig. 5b and Supplementary Fig. 21a) were measured with a UV-Vis-NIR spectrophotometer Agilent, model Cary 5000, equipped with an integrating sphere with the samples placed in the reflectance port (scan rate of 600 nm/min).

The spectra were evaluated by the principal component analysis to determine if sufficient differences and/or grouping of different samples were evident. These differences can be used from the basis of an automated classification and sorting scheme during the recycling process. The PCA analysis was performed using package "stats" in R environment (v. 3.6.1)[29]. The reflectance spectral data were converted to z-scores prior to PCA analysis (Supplementary Fig. 21a). The PCA showed (Supplementary Fig. 21b) that 65% of the variation between the near-IR spectra was accounted by the first principal component (PC1) and 25% by the second principal component (PC2). The PCA scatter plots (Fig. 5c and Supplementary Fig. 21c) exhibit clear clustering of the spectral data from LLDPE fibers and HDPE fibers, which are well separated from the corresponding data for cotton and polyester. The PCA results shown that different types of PE fibers (including dark-colored ones) can be distinguished from each other and from other textile polymers by their near-IR spectra. Many other inorganic nanoparticles that do not obscure the PE near-IR fingerprints can be introduced via spin-dying procedure as colorants into PE fibers and textiles.

## 14. Mechanical testing and improvement of PE fibers and fabrics

To test the mechanical properties and the durability of the PE fibers and woven PE fabrics we have performed the tensile strength and the abrasion resistance testing.

Abrasion testing has been done on the Martindale M235 Abrasion Tester according to the ASTM D 4966 standard. Circular specimens of the PE and conventional textiles of 38 mm in diameter have been mounted flat and rubbed with a piece of worsted wool cloth. A force of 9 kPa has been applied to the top of the specimen to hold it against the abradant. Each fabric has been subjected to 10,000 cycles of rubbing motion with the standard speed of 47.5 RPM under ambient parameters of 58%RH and 72°F. The results are summarized in the Supplementary Fig. 22a-c. The woven PE fabric exhibited larger mass reduction than the woven cotton and polyester textiles.

However, knitted fabric samples made from the same yarn as the woven PE fabric demonstrated much better resistance to abrasion (see Supplementary Fig. 22a,c). This demonstrated that an additional level of control via the fabric composition can be used to improve wearability properties of the PE fabrics composed of the LLDPE fibers. In the following, we show that the fabrics mechanical properties can be further improved by increasing the molecular weight of the PE material used for the PE yarn spinning.

Tensile strengths of the PE fibers and yarns have been measured by using Instron tensile test with 38 mm gauge and 60 mm/min strain rate (Instron 68SC-05 with a 10N load cell certified for use from 0.04N to 10N with an accuracy of +/- 0.5%). Neither of the PE fabric samples nor cotton and polyester fabrics could be ripped by using the maximum load of 10N. To test individual monofilament PE fibers, we used a KLA T150 UTM tester (a nano-tensile tester for single fiber measurement with a maximum load of 500mN). Typical stress-strain curves for LLDPE monofilaments are shown in Supplementary Fig. 23. To explore the range of the tensile strength achievable in the polyethylene fibers of different PE polymer chain lengths, we fabricated monofilament fibers composed on 100% HDPE material and a mix of 90% HDPE and 10% of UHMWPE. The latter fiber was too strong to be broken by the Instron tester at the maximum load, while the former exhibited higher strength than the LLDPE monofilaments extracted from the multi-filament yarn. The results are summarized in the Supplementary Table 5, together with the literature data for polyester and nylon fibers as well as the UHMWPE Spectra 1000 (which is one

of strongest commercially available polymer fibers, fabricated by a gel-spinning process). The data demonstrate that (i) the PE fibers fabricated by the standard melt extrusion process can have a greatly variable strength that can be engineered by controlling the material composition of the fiber, and (ii) even the weakest LLDPE fibers can be woven into a strong fabric structure suitable for wearable applications.
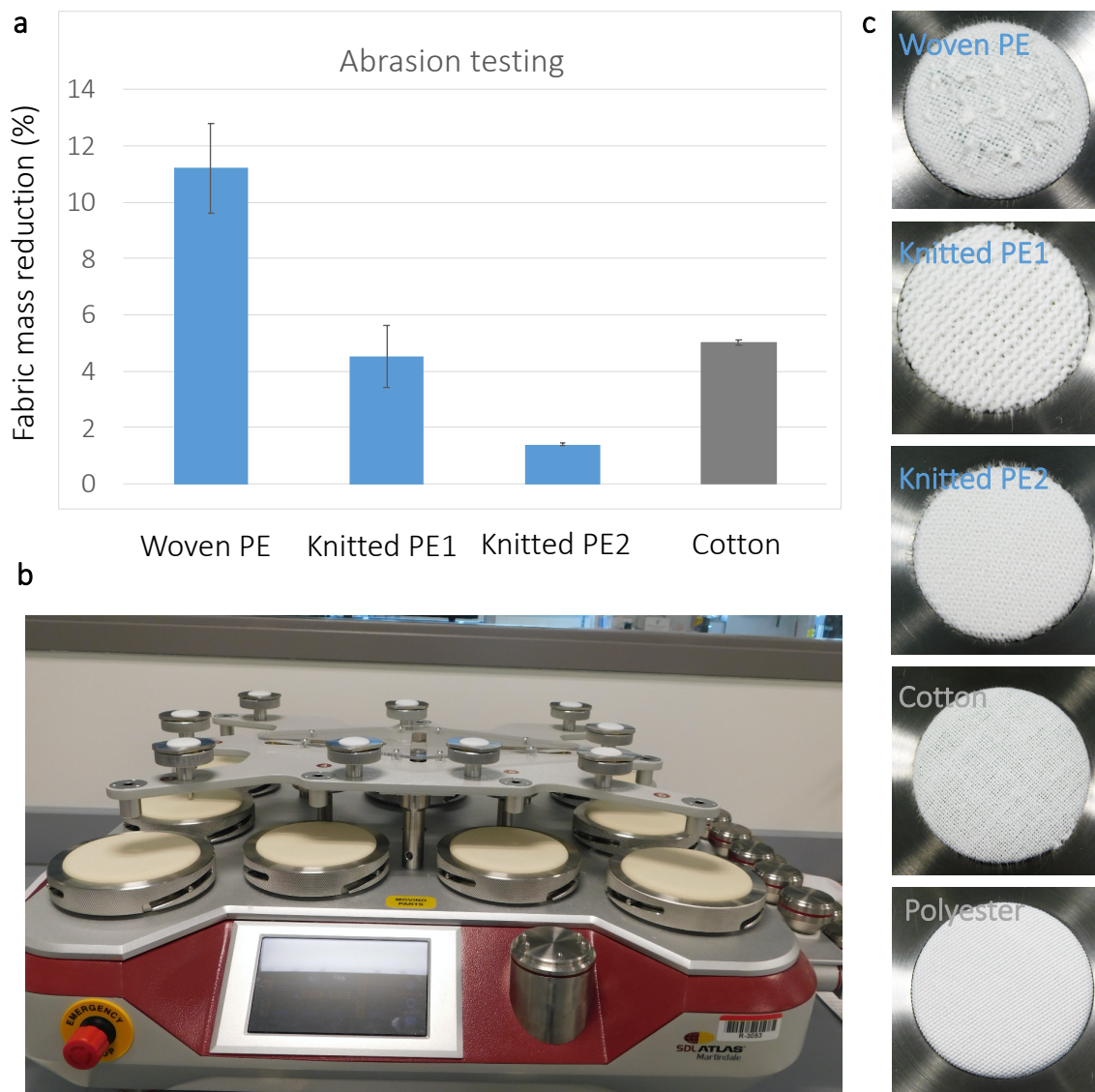
Supplementary Figure 22. Abrasion testing of the PE and conventional fabrics. (a) Mass reduction (in %) of PE fabrics of different composition (one woven and two different knitted samples) after 10,000 cycles of abrasion with the force of 9 kPa. The corresponding data for a woven cotton fabric sample is shown for comparison. A polyester sample did not exhibit mass reduction after testing under the same conditions. (b) A photograph of the Martindale abrasion tester. (c) Photographs of different fabrics samples after 10,000 cycles.
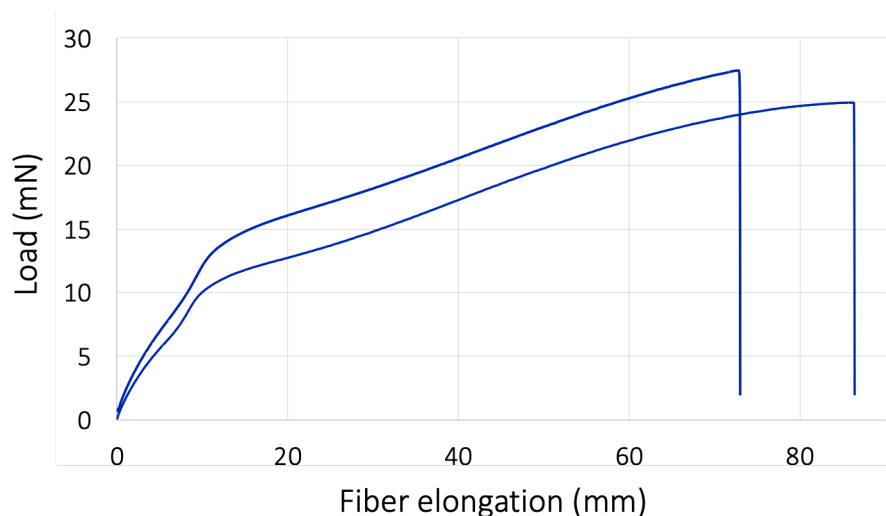
Supplementary Figure 23. Typical stress-strain curves for LLDPE monofilaments extracted from the LLDPE yarn.

Supplementary Table 5. Tensile strength of the melt-spun PE fibers.

Material	Monofilament, dpf	Young modulus, gf/den	Max tenacity, gf/den	Tensile strain at break, %
LLDPE	2	5.84	1.33	207.9
HDPE	6.78	23.1	3.715	84.06
HDPE/UHMWPE	30	205	(12.74+)	(1067+)
Polyester		120-150	4.5-6.5	7-15
Nylon		34-50	4.3-8.8	16-20
Spectra 1000 (UHMWPE)	1.9	1550	43	2.9

15. Crystallinity and thermal properties of PE fibers

We summarized the data on the PE fiber thermal properties and crystallinity in Supplementary Table 6. Crystallinity of the PE fibers studied in this work has been measured via differential scanning calorimetry (DSC) and via the wide-angle X-ray scattering (WAXS) technique.

Differential scanning calorimetry (DSC) measurements were performed using a calorimeter model Discovery from TA Instruments. Samples of ~1 mg were weighed with a precision balance and encapsulated in aluminum pans of known mass. An identical empty pan was used as a reference. Nitrogen was purged at a rate of 50 ml/min. Heating-cooling-heating cycles in the range from −40 to 160 °C were applied with heating and cooling rates of 10 °C/min. Supplementary Figure 24a shows typical results of the differential scanning calorimetry (DSC) measurements of the LLDPE

and HDPE/UHMWPE fibers, with the melting points of fibers manifested as endothermic dips in the plots. HDPE/UHMWPE fibers exhibit slightly higher melting temperature relative to that of the LLDPE fibers, and higher degree of crystallinity. The narrower temperature bandwidth of the endothermic dips of the HDPE/UWMWPE fibers also indicates higher homogeneity of their crystalline domains in size and internal structure.

We additionally used the SAXSLAB system with a Rigaku 002 microfocus X-ray source and a DECTRIS PILATUS 300K detector to perform the WAXS measurements on the fibers. The WAXS measurements are taken as a function on scattering angle, 2θ, from the forward direction of the radiation with wavelength (CuKα1 = 1.5409Å). Plots of relative intensity as a function of scattering angle for the LLDPE fibers and the HDPE/UHMWPE fibers are shown in Supplementary Fig. 24b. The crystallinity values for both types of fibers have been calculated as the ratio of the area of the crystalline peaks and area of the combined amorphous and crystalline peaks in the corresponding intensity plots.

Azimuthal scans have also been taken at constant values of 2θ, and the degree of the crystalline orientation has been estimated from the intensity distribution of the diffraction on the Debye ring by using the Hermans orientation function, $f = \frac{1}{2}(3\langle\cos^2\phi\rangle - 1)$. The results revealed random/parallel orientation of crystallites in the LLDPE fibers and random/perpendicular orientation in the HDPE/UHMWPE fibers (relative to the fiber axis). Note that $f = 1$ corresponds to the parallel orientation, $f = 0$ to random, and $f = -0.5$, to perpendicular.

Supplementary Table 6. Thermal properties and crystallinity of PE fibers.

Fiber material	Density, g/cm³	ΔH, (J/g)	Melting temperature, ºC	Crystallinity (from DSC), %	Crystallinity (from WAXS), %	Orientation function
LLDPE	0.93	151.28	122	52.3%	52%	0.267
HDPE/ UHMWPE	0.97	174.35	124.6	60.3%	59%	-0.104
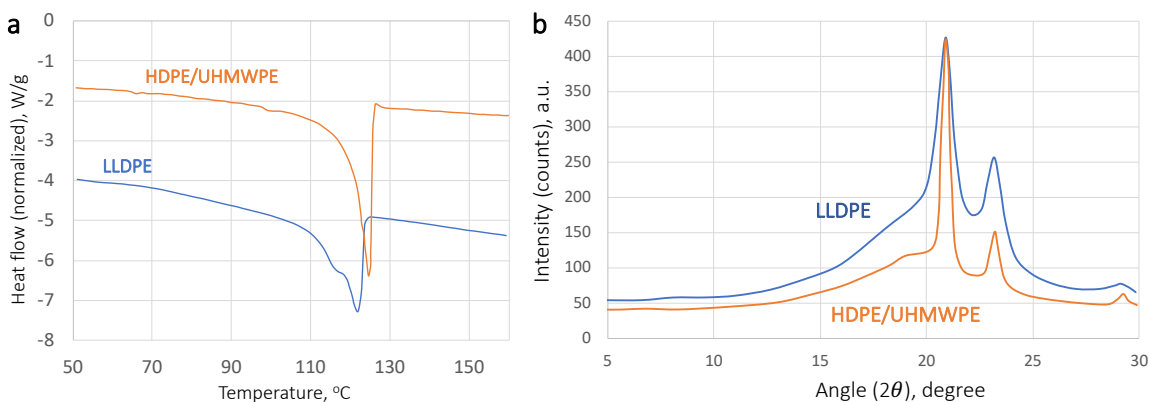
Supplementary Figure 24. Results of the differential scanning calorimetry (DSC) and wide-angle X-ray scattering (WAXS) measurements of the PE fibers. (a) DSC temperatures scans of LLDPE (blue) and HDPE/UHMWPE fibers (orange). (b) WAXS spectra of LLDPE (blue) and HDPE/UHMWPE fibers (orange).

Exposure to elevated temperatures in the range 50-100 ºC caused slight visible shrinkage of the yarn and fabric. However, after initial shrinkage, longer exposure to the high yet below-melting

temperatures (~80 °C) did not result in additional shrinkage, suggesting a mechanism for thermal curing of the PE fibers and yarn during production to avoid fabric shrinkage during the use phase. Additional effects of the thermal curing on the crystallinity and orientation of the PE fibers made from different types of raw PE materials under different drawing conditions will be evaluated in the course of ongoing and future studies.

16. Handle-feel properties of woven PE textiles

We have used the fabric touch tester (FTT) equipment (SDL Atlas) at the US Army CCDC Soldier Center to evaluate the handle feel properties of the woven PE fabrics and compare them to the conventional natural and synthetic woven textiles and the non-woven PE films (NyCo is a US Army uniform textile composed of nylon 6,6 and cotton, which is shown for comparison). The results are summarized in the Supplementary Table SX, and include the following parameters:

- Bending Work (gf·mm·rad) - Work needed to bend the fabric specimen (average for the inner and outer side of the textile)

- Compression Work (gf·mm) - Work needed to compress the specimen (average for the inner and outer side of the textile)

- Compression Recovery Rate (%) - Percentage of thickness changes after compressed (average for the inner and outer side of the textile)

- Surface Friction Coefficient - Friction coefficient on surface with ribbed metal plate (shown separately for the inner and outer side of the textile)

Supplementary Table 7. Handle feel properties of fabrics.

| Material	Bending work, gf·mm·rad	Compression work, gf·mm	Compression recovery rate, %	Inner friction coefficient	Outer friction coefficient	Thermal flux, W/m^2
Woven PE	504	513	0.43	0.45	0.44	1100
Nonwoven Tyvek	225	880	0.26	0.36	0.48	1105
Woven cotton	509	920	0.52	0.36	0.35	837
Woven linen	650	815	0.67	0.54	0.37	1068
Woven polyester	653	786	0.78	0.26	0.29	886
NyCo	843	1248	0.61	0.25	0.25	985

The data in Supplementary Table 7 demonstrate that woven PE fabrics exhibit high softness and flexibility relative to other tested materials, with high recovery after compression. Both woven and

non-woven PE textiles are also shown to remove heat more efficiently (as have been previously predicted and demonstrated). The high denier count of our woven fabric translates to the higher friction coefficient, comparable in value to the friction coefficient measured for a woven linen textile.

It should be noted that all the parameters shown in Supplementary Table 7 can be further engineered via fabric composition (e.g., yarn plying and using different knitted or woven patterns).

17. Scaling up fabrication of PE textiles and garments

We demonstrated that PE yarns can not only be produced on a standard melt-spin equipment but can also be knitted and woven by using standard industrial looms and computerized knitting machines. The images in Supplementary Fig. 25 demonstrate fabrics of different knitting and woven patterns that have been produced from the multi-filament LLDPE yarns and used to make a range of different garments, including full-size knitted sweaters and fully-knitted socks. The woven PE textile extensively studied in this work has been fabricated by Shingora Ldt. (India), and the knitted fabrics and garments shown in Supplementary Fig. 25 have been fabricated by the Advanced Functional Fabrics of America (AFFOA, Cambridge, MA). The material offers a silky touch feeling, wrinkle resistance, as well as variable stretching and drapery properties, which can be controlled by the knitting/weaving pattern of the fabric.
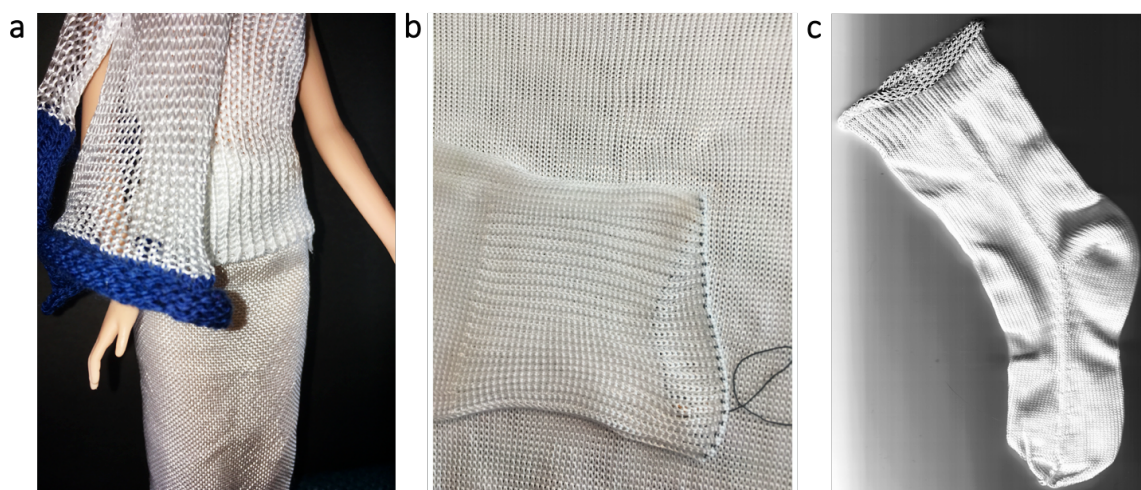
Supplementary Figure 25: PE fabrics and garments produced in a variety of fabric patterns and garment designs. (a) A small-scale outfit composed of a plane-woven PE skirt, and knitted PE top and scarf (fits a 12 inch-sized doll). (b) An adult-size knitted PE sweater. (c) A child-size sock knitted from a PE yarn.

18. Evaluation of the expanded uncertainty of measurements

The expanded uncertainty of experimental measurements can be estimated as:

$$U = k\sqrt{u_A^2 + u_B^2}\,, \tag{35}$$

where u_A expresses the uncertainty component estimated by statistical analysis of the measured values (type A), u_B refers to the uncertainty components evaluated by other means (type B), *a priori* information of the instruments such as calibration, accuracy and resolution, and $k = 2$ is the coverage factor, in accordance to the NIST standard on uncertainty evaluation[30]. The error bars reported in the figures present a $\pm U$ interval, which, for every measure, is computed as described in the following sections.

18.1. Yarn porosity

The expanded uncertainty of the yarn porosity is evaluated as:

$$U_\phi = k \sqrt{\left(S_0 \cdot u_{a_1}\right)^2 + u_{a_0}^2 + \left(a_1 \cdot \frac{u_{S_0}}{2\sqrt{3}}\right)^2 + u_{fit}^2}, \tag{36}$$

where $S_0 = 0.5$ is the sensitivity level chosen to evaluate the yarn porosity from the microCT images, u_{a_1} and u_{a_0} are the uncertainty of the fitting parameters evaluated via the least squares method, $u_{S_0} = 0.1$ is the uncertainty of the sensitivity S_0, considered as uniformly distributed. u_{fit} is the contribution to the uncertainty of the linear fit computed as the root mean squared error:

$$u_{fit} = \sqrt{\frac{\sum_{i=1}^{n_{tot}} \left((a_1 S_i - a_0) - \phi|_{S_i}\right)^2}{n_{tot} - 2}}, \tag{37}$$

where $n_{tot} = 200$ is the total number of sensitivities computed in the range from 0.4 to 0.6, and $\phi|_{S_i}$ is the porosity computed by the "imbinarize" MATLAB function for the given sensitivity level S_i.

18.2. Position of the water front

The standard uncertainty on the *i-th* measurement of the height $h_{\Delta t,i}$ reached by the water front, with $i = (1; \dots; 6)$ is evaluated as:

$$u_{h_{t,i}} = \sqrt{\left(\frac{u_s}{2\sqrt{3}}\right)^2 + \left(\frac{u_{f_i}}{2\sqrt{6}}\right)^2}, \tag{38}$$

where $u_s = 2$ mm is the contribution to the uncertainty of the dipping length, considered as uniformly distributed, and u_f is the thickness of the water front, whose probability distribution is considered as triangular. The uncertainty contribution of the resolution of the caliber is negligible.

The expanded uncertainty on the averaged value of the final height is evaluated as:

$$U_h = k \sqrt{\frac{\sum_i^N u_{h_{t,i}}^2}{N^2} + \frac{R^2}{N}}, \tag{39}$$

where $R = \frac{\left(\max\left(h_{t,i}\right) - \min\left(h_{t,i}\right)\right)}{2}$ is the estimation of the statistical uncertainty of the $N = 6$ measurements performed on each material.

18.3. Contact angle

The method adopted to compute the contact angle is based on the experimental evaluation of the reduced length and height of the droplets on fibers from optical images of a droplet on a fiber, respectively, expressed as:

$$l = \frac{L}{r}, \qquad t = \frac{T}{2r},$$ (40)

where L is the maximum length of the droplet, r is the fiber radius, and T is the droplet thickness (see Fig. 2c), each measured in pixels from the images acquired. The uncertainty estimated for all the three measures is $u_{px} = 8$ px, considered as uniformly distributed. The model employed to compute the contact angle from the observation of each droplet is non-linear, thus these uncertainties cannot be easily propagated. Therefore, the method is applied 4,000 times for each image acquired, where, at each iteration j, the values of r_j, L_j and T_j used are randomly generated from a normal distribution with respective mean values r, L and T, and standard deviation $u_{px}/2\sqrt{3}$. The average contact angle $\bar{\theta}_i$ is estimated as:

$$\bar{\theta}_i = \frac{\sum_{j=1}^{N} \theta_j}{N},$$ (41)

with $N = 4000$, and the uncertainty $u_{\bar{\theta}_i}$ as the standard deviation of the sample. The size of N is chosen so that $\bar{\theta}_i$ and $u_{\bar{\theta}_i}$ have a variation lower than 10^{-2} if the procedure is repeated for the same combination of r, L and T. The method is applied to every evaluation of the contact angle, which is then averaged for every type of fiber analyzed, so that:

$$\theta = \frac{\sum_{i=1}^{N} \bar{\theta}_i}{N}, \qquad U_\theta = k \sqrt{\frac{\sum_i^{N} u_{\bar{\theta}_i}^2}{N^2} + \frac{R^2}{N}},$$ (42)

where $N \geq 16$ for the all the fibers tested, and R is the standard deviation of the sample.

18.4. Evaporation tests

During the evaporation tests, the mass of the setup is acquired with a sampling frequency of 1 sample every 2 minutes. The percentage of drying mass $L(t)$ is computed as:

$$L(t) = 100 \cdot \frac{M(t) - M_0 + m_D}{m_D},$$ (43)

where $M(t)$ is the time-dependent mass of the setup, M_0 is the weight of the setup at the beginning of the test, and m_D is the mass of the water droplet. m_D is evaluated as the difference between the weight of the setup before and after the application of the water droplet, averaging the values of 5 reads with a sampling frequency of 1 sample/s. Therefore, the uncertainty on L can be estimated as:

$$u_{L(t)} = \sqrt{\left(\frac{u_{M(t)}}{m_D\sqrt{3}}\right)^2 + \left(\frac{u_{M_0}}{m_D\sqrt{3}}\right)^2 + \left(u_{m_D}\frac{M_0 - M(t)}{m_D^2}\right)^2},$$ (44)

where $u_{M(t)} = u_{M_0} = 2$ mg, considered as uniformly distributed, and $u_{m_D} = 5$ mg, considered as uniformly distributed.

18.5. Temperature

The uncertainty of the points composing the temperature curves in Fig. 3f-g and Supplementary Figs. 19 and 20 can be evaluated as:

$$U_T = k \sqrt{\left(\frac{u_r}{\sqrt{3}}\right)^2 + \left(\frac{u_{TM}}{2}\right)^2 + \left(\frac{u_{FSR}}{2}\right)^2} , \qquad (45)$$

where $u_r = 10^{-3}$ °C is the contribution of the logger resolution, considered as uniformly distributed, $u_{TM} = 10^{-2}$ °C and $u_{FR} = 0.38$°C are respectively the contribution of the thermistor sensitivity and the accuracy on the full-scale range reading of the used thermistor, both considered as normally distributed with a coverage factor $k = 2$.

19. Supplementary References

1. http://inserco.org/en/statistics.
2. alibaba.com. No Title.
3. Qin, Y. (Michelle). *Global Fibres Overview*. (2014).
4. Geyer, R., Jambeck, J. R. & Law, K. L. Production, use, and fate of all plastics ever made. *Sci. Adv.* **3**, e1700782 (2017).
5. https://www.icis.com/explore/commodities/chemicals/polyethylene/.
6. Higg Materials Sustainability Index - https://msi.higg.org/.
7. Abràmoff, M. D., Magalhães, P. J. & Ram, S. J. *Image Processing with ImageJ Second Edition*. *Biophotonics International* vol. 11 (Laurin Publishing, 2004).
8. Nečas, D. & Klapetek, P. Gwyddion: An open-source software for SPM data analysis. *Central European Journal of Physics* vol. 10 181–188 (2012).
9. Gennes, P.-G. de, Brochard-Wyart, F. & Quere, D. *Capillarity and Wetting Phenomena.pdf*. (2002).
10. Carroll, B. J. Accurate measurement of contact angle, phase contact areas, drop volume, and Laplace excess pressure in drop-on-fibre systems. *J. Colloid Interface Sci.* **57**, 488–495 (1976).
11. Owens, D. K. & Wendt, R. C. Estimation of the surface free energy of polymers. *J. Appl. Polym. Sci.* **13**, 1741–1747 (1969).
12. Faghri, A. & Zhang, Y. *Transport Phenomena in Multiphase Systems*. *Transport Phenomena in Multiphase Systems* (2006).
13. Kwok, D. Y. & Neumann, A. W. *Contact angle measurement and contact angle interpretation*. *Advances in Colloid and Interface Science* vol. 81 (1999).
14. Hata, T., Kitazaki, Y. & Saito, T. Estimation of the Surface Energy of Polymer Solids†. *J. Adhes.* **21**, 177–194 (1987).
15. McHale, G. & Newton, M. I. Global geometry and the equilibrium shapes of liquid drops on fibers. *Colloids Surfaces A Physicochem. Eng. Asp.* **206**, 79–86 (2002).
16. Extrand, C. W. & Moon, S. I. Contact angles on spherical surfaces. *Langmuir* **24**, 9470–9473 (2008).

17. Westerlind, B. S. & Berg, J. C. Surface energy of untreated and surface-modified cellulose fibers. *J. Appl. Polym. Sci.* **36**, 523–534 (1988).
18. McHale, G., Käb, N. A., Newton, M. I. & Rowan, S. M. Wetting of a high-energy fiber surface. *J. Colloid Interface Sci.* **186**, 453–461 (1997).
19. Kralchevsky, P. A., Paunov, V. N., Ivanov, I. B. & Nagayama, K. Capillary meniscus interaction between colloidal particles attached to a liquid-fluid interface. *J. Colloid Interface Sci.* **151**, 79–94 (1992).
20. Sanchis, M. R., Blanes, V., Blanes, M., Garcia, D. & Balart, R. Surface modification of low density polyethylene (LDPE) film by low pressure O2 plasma treatment. *Eur. Polym. J.* **42**, 1558–1568 (2006).
21. Drnovská, H., Lapčík, L., Buršíková, V., Zemek, J. & Barros-Timmons, A. M. Surface properties of polyethylene after low-temperature plasma treatment. *Colloid Polym. Sci.* **281**, 1025–1033 (2003).
22. Koopal, L. K. Wetting of solid surfaces: Fundamentals and charge effects. *Adv. Colloid Interface Sci.* **179–182**, 29–42 (2012).
23. Moreno-Villa, V.M.; Ponce-Velez, M.A.; Valle-Jaime, E.; Fierro-Chavez, J. L. . Effect of surface charge on hydrophobicity levels. *IEE Proceedings-Generation, Transm. Distrib.* **145**, 6834–6839 (1998).
24. Karaki, M. *et al.* A Comparative Analytical, Numerical and Experimental Analysis of the Microscopic Permeability of Fiber Bundles in Composite Materials. *Int. J. Compos. Mater.* **7**, 82–102 (2017).
25. Berdichevsky, A. L. & Cai, Z. Preform permeability predictions by self-consistent method and finite element simulation. *Polym. Compos.* **14**, 132–143 (1993).
26. Princen, H. M. Capillary phenomena in assemblies of parallel cylinders. II. Capillary rise in systems with more than two cylinders. *J. Colloid Interface Sci.* **30**, 359–371 (1969).
27. Princen, H. M. Capillary phenomena in assemblies of parallel cylinders. I. Capillary rise between two cylinders. *J. Colloid Interface Sci.* (1969) doi:10.1016/0021-9797(69)90379-8.
28. Wold, S., Esbensen, K. & Geladi, P. Principal component analysis. *Chemom. Intell. Lab. Syst.* **2**, 37–52 (1987).
29. Core Team, R. *R: A language and environment for statistical computing. R Foundation for Statistical Computing*. (2019).
30. Taylor, B. N. & Kuyatt, C. E. NIST Technical Note 1297 1994 Edition, Guidelines for Evaluating and Expressing the Uncertainty of NIST Measurement Results. *Natl. Inst. Stand. Technol.* 1–20 (1994).